Mesoscale and microscale shock effects in the LL6 S4 chondrites Saint-Séverin and Elbert: A tale of two breccias*

Richard C. Hugo[1], Alex M. Ruzicka[1], Alan E. Rubin[2]

[1] Portland State University, Department of Geology and Cascadia Meteorite Laboratory, 17 Cramer Hall, 1721 SW Broadway, Portland, OR, USA

[2] Institute of Geophysics and Planetary Physics, University of California, Los Angeles, CA, USA

November 30, 2018
Revised April 9, 2019

Submitted to *Meteoritics & Planetary Science*

*Paper dedicated to the memory of Christine Floss

Abstract. Saint-Séverin and Elbert, two LL6 chondrite breccias, were systematically studied to evaluate multiple deformation effects on spatial scales ranging from thin-section (mesoscale) to micron-submicron (microscale) using optical microscopy (OM), electron backscatter diffraction (EBSD), and transmission electron microscopy (TEM). The different techniques provide consistent results but have complementary strengths, together providing a powerful approach to unravel even complex impact histories. Both meteorites have an S4 conventional shock stage, but interclast areas are more deformed, and clasts are more deformed in Elbert than in Saint-Séverin. TEM and EBSD data provide compelling evidence that Saint-Séverin experienced significant shock deformation while already hot, and cooled rapidly afterwards, as a result of a major, possibly disruptive impact on the LL chondrite parent body ~4.4 Ga ago. In contrast, Elbert was shocked from a cold initial state but was heated significantly during shock, and cooled in a localized hot impact deposit on the LL asteroid. Both meteorites probably were shocked at least twice; data for Saint-Séverin are best reconciled with a three-impact model.

INTRODUCTION

Recent work suggests that impact conditions may have differed dramatically for the asteroidal parent bodies of ordinary chondrites at different times and/or locations. Some ordinary chondrites were shocked while already hot (Friedrich et al., 2013, 2014; Ruzicka et al., 2015), and were annealed following deformation (Ruzicka et al., 2015; Friedrich et al. 2017; Ruzicka and Hugo, 2018). Post-shock annealing of such chondrites helped lessen plastic deformation in olivine and decrease shock stages (Ruzicka et al., 2015; Ruzicka and Hugo, 2018), in agreement with previous suggestions for various

chondrites (Rubin, 2004; Rubin and Jones, 2003). Further, post-shock annealing may have resulted in metal grain growth that diminished the extent of shape preferred orientations (SPOs) of metal established by shock compaction (Friedrich et al., 2017). Hot-deformed and annealed chondrites could have formed by collisions between metamorphosing planetesimals in the early solar system (Ruzicka et al., 2015; Ruzicka and Hugo, 2018), which became more-or-less impact-scrambled as a result of the impacts (Scott et al., 2014; Ganguly et al., 2013, 2016; Blackburn et al., 2017). In contrast, other ordinary chondrites were strongly shocked while cold, and were little-annealed afterwards (Ruzicka et al., 2015; Friedrich et al. 2017; Ruzicka and Hugo, 2018). Cold-deformed and little-annealed chondrites could have formed by collisions on cold parent bodies at a later time in solar system history (Ruzicka et al., 2015; Ruzicka and Hugo, 2018).

Deciphering the impact record of 4.56 Ga-old chondrites that were subject to a long history of impact bombardment is potentially complicated by the effects of multiple impacts and brecciation. Multiple impacts could be additive in shock damage, with significant late impacts effectively overprinting and obliterating evidence for earlier ones. Different clasts might record different histories, or not, depending on the extent of overprinting during the impact events that created breccias.

An especially large proportion of LL chondrites are breccias (Keil, 1982; Bischoff et al., 2018a). Such LL breccias offer an opportunity for detailed study to evaluate potential complexities caused by repeated impacts or brecciation effects. One previous LL6 breccia, Miller Range (hereafter MIL) 99301, was investigated in detail and found to contain a shock melt clast of differing deformation character than the host

(Ruzicka and Hugo, 2018). Here, we studied two additional representative LL6 chondrites—Saint-Séverin and Elbert—using methods previously used for type 6 ordinary chondrites (Ruzicka et al., 2015; Ruzicka and Hugo, 2018), from thin-section (mesoscale) to transmission electron microscope (TEM) accessible microscales. Elbert and Saint-Séverin were both classified as shock stage (Stöffler et al., 1991) S2 by Rubin (2004). Both meteorites and Elbert specifically were described on the basis of potential shock indicators as candidates of having once been shocked to higher (S4 or S5) levels, annealed to S1, and then re-shocked to S2 (Rubin, 2004).

Among the two meteorites, Saint-Séverin has received far more study. This includes two TEM investigations (Ashworth and Barber, 1977; Leroux et al., 1996), dating (Hohenberg et al., 1981), cooling rate analysis based on metal and silicate zoning (Willis and Goldstein, 1983; Ganguly et al., 2016), and a combined microtomography (μCT), porosity, optical microscopy (OM) study (Friedrich et al., 2017).

The two TEM studies for Saint-Séverin come to somewhat different interpretations regarding microstructures. Leroux et al. (1996) found evidence for two shock events with an intervening episode of metamorphism. According to these researchers, an early shock event injected Fe-FeS melt into fractures in silicates. This was followed by static heating at high temperature (700-900 °C) to heal fractures and produce "blackened" silicates with Fe-FeS inclusions embedded in the silicates, and to produce curved free dislocations and some recovery-controlled subgrain boundaries in olivine. Finally, a later shock event that may have ejected Saint-Séverin from its parent body occurred under cold conditions to produce straight, free screw dislocations in olivine. In contrast, Ashworth and Barber (1977) suggested mild, early impact during cooling from

metamorphic temperatures (≥500 °C) to produce kink bands and curved dislocations, followed by limited dislocation recovery, constituting some of the first evidence for deformation occurring at elevated temperatures in a chondrite.

In other research on Saint-Séverin, Hohenberg et al. (1981) found two different Ar plateau ages for coarser-grained "dark" (~4.42 Ga) and finer-grained "light" (~4.38 Ga) portions, with an apparently significant age difference of 37 ± 13 Ma between the two. Ganguly et al. (2016) used zoning profiles in silicates (lack of zoning) and literature metallographic data to model rapid cooling (~200 °C/ka) of Saint-Séverin from high temperature, interpreted as a result of collisional disruption of the LL parent body while it was hot, followed by burial to cool more slowly at low (<500 °C) temperatures. Friedrich et al. (2017) suggested a model of multiple impacts, involving (1) an early shock of moderate intensity, with shock stage S3-S4 and limited post-shock annealing, possibly at ~4.42 Ga ago, (2) brecciation that destroyed whatever metal foliation was established by the first shock event, and (3) a later weak (S2) shock, possibly at ~4.38 Ga ago, that re-established a modest metal foliation and re-lithified the meteorite.

There were four overall goals for this study. These included: 1) evaluating how Saint-Séverin and Elbert as a whole and their breccia components compare to each other and to previously studied meteorites in terms of deformation extent, deformation temperature, and post-shock annealing; 2) assessing evidence for multi-stage deformation and the extent to which earlier shock episodes are overprinted by later events; 3) resolving conflicting evidence for the shock history of Saint-Séverin; and 4) determining how the overall shock and thermal histories of these meteorites relate to impact and metamorphic processes on the LL chondrite asteroid. We focused on olivine as it is the

most abundant mineral in chondrites and has a well characterized deformation response. We also considered troilite as a potentially useful indicator of pre-ambient deformation temperature (Schmitt, 2000) and direction of shock compaction (Ruzicka and Hugo, 2018).

SAMPLES AND METHODS

Samples for study included three doubly polished thin sections of Saint-Séverin (NMNH 2608, CML 0665-1, CML 0665-2B), and one of Elbert (CML 0479-B), the latter of which contained two separate pieces (hereafter referred to as Elbert A and Elbert B). These samples are curated at the National Museum of Natural History (NMNH) in Washington, D.C., and the Cascadia Meteorite Laboratory (CML) at Portland State University (PSU). All sections were used for optical microscopy (OM), and CML 0665-2B and CML 0479-B were used for electron backscatter diffraction (EBSD) and transmission electron microscopy (TEM). For EBSD analysis, sections with original microprobe-grade polish were additionally prepared to obtain a better-quality polish by hand polishing with colloidal silica solution (Buehler Mastermet, product 40-6370-006) for 30-40 minutes, followed by evaporative carbon coating to ~4 nm thickness.

Using OM, a weighted shock stage was assigned to each meteorite according to the method of Jamsja and Ruzicka (2010). In this method, individual olivine grains are each assigned a shock score consistent with the quantitative deformation measures of extinction misorientation angles and number of planar fracture sets (Stöffler et al., 1991; Schmitt and Stöffler, 1995; Schmitt, 2000), and recrystallization of olivine is taken as being indicative of shock stage S6 (Bischoff et al., 2018b). The weighted shock stage is given as the average of the individual scores, and heterogeneity is indicated by ±1σ

values. Conventional shock stage is assigned as the highest shock score that has ≥25% of the grains (Stöffler et al. 1991). A different conventional shock stage is possible if quantitative measures are not considered, or if an alternative scheme is followed (e.g., Stöffler et al., 2018).

EBSD mapping was performed on a Zeiss Sigma VP-FEG-SEM with HKL Nordlys Nano detector and Oxford Instruments AZtec 3.2 software at the Center for Electron Microscopy and Nanofabrication (CEMN) at PSU. The SEM was operated at 20 kV accelerating voltage and 11 nA probe current, with the specimen tilted at 70°. Thin-section scale Large Area Map (LAM) EBSD data were acquired at 4 μm step size for Saint-Séverin and Elbert A, and at 2 μm step size for Elbert B. These covered an area of approximately 88.6 mm^2 (12.3 x 7.2 mm across), 49 mm^2 (7.1 x 6.9 mm) and 15.5 mm^2 (4.3 x 3.6 mm), respectively. Five Targeted Area Maps (TAMs) in Saint-Séverin and three in Elbert were mapped at 0.9-1.4 μm step size to show areas of interest in more detail. In addition, a small TAM with high spatial resolution (0.2 μm step size) of a Saint-Séverin interclast area was obtained prior to TEM work. Crystal orientation precision and detection limit for olivine in these maps is ≤0.1-0.2° (Ruzicka and Hugo, 2018).

EBSD data were processed using HKL Channel5 software. Grains were identified as the same phase with at least five contiguous pixels, using a 15° critical misorientation (i.e., grains with boundaries ≥15° are treated as separate grains) and boundary completion to 0.5°. As reliable OM measurements for shock deformation in olivine are best made on grains larger than 50 μm across, datasets were analyzed according to olivine grains of all sizes as well as for grains <50 μm and >50 μm in effective diameter (d, corresponding to the diameter of a circular grain with the same area as measured). To characterize plastic

deformation extent for olivine, standard EBSD metrics (Wright et al., 2011) including Grain Orientation Spread (GOS, the average misorientation within a grain), Maximum Orientation Spread (MOS, the maximum misorientation within a grain), Kernal Average Misorientation (KAM, the average pixel-to-pixel misorientation within a grain), and Grain Reference Orientation Deviation angle (GROD angle, the misorientation relative to the average grain orientation) were determined. As GOS (unlike KAM) is relatively insensitive to sampling step size (Wright et al., 2011) and is a relatively robust deformation parameter (Ruzicka and Hugo, 2018), GOS was used as the primary measure of plastic deformation extent in olivine. Previous work (Ruzicka and Hugo, 2018) showed that for larger (d>50 μm) grains, mean GOS olivine values of ~0.5-1.5° are associated with weak shock (shock stage S1), whereas mean values of ~3-4° are associated with strong shock (shock stage S4-S5). The mean/median value of GOS, which is related to the skewness of GOS distributions, was determined for olivine grains with d>50 μm and can be interpreted as a post-deformation annealing parameter (Ruzicka and Hugo, 2018). EBSD slip system analysis was performed using Crystal Rotation Axis (CRA) figures, which show the probability distribution (represented by Multiples of Uniform Distribution, or MUD, values) of misorientation axis directions in an olivine crystal frame. A simple inferred deformation temperature parameter, valid for low to intermediate shock temperatures, is $f_{<001>} + f_{<010>}$, where $f_{<hkl>}$ is the normalized CRA-MUD value at the three low-index hkl poles for 2-10° misorientations (Ruzicka and Hugo, 2018). The numeric value of deformation temperature parameter is the proportion of misorientation axis directions other than that expected for low-temperature deformation. The extent of Lattice Preferred Orientations (LPOs) in troilite and olivine

were evaluated based on pole figure plots for EBSD LAM data. Previous work showed that $\{0001\}_{troilite}$ and $<001>_{olivine}$ have preferred orientations in some strongly shocked chondrites, which reflect an overall shock compression direction (Ruzicka and Hugo, 2018). To analyze spatial variations on clast scales, LAM datasets were segregated into spatial subsets corresponding to individual clasts and interclast regions (Fig. 1). TAMs with higher spatial resolution were also considered. All LPO analysis was performed on the basis of 1 point per grain for grains of all sizes. In this manuscript we consider whether LPOs signify deformation based on the pole figure patterns, grain orientation patterns in orientation maps, the strength of the LPO patterns based on MUD values, and the number of grains for the minerals. In our data, MUD values for both LPOs and CRA diagrams tend to be low; thus they are only considered significant when positively correlated and/or confirmed with other data.

TEM specimens were prepared by Focused Ion Beam (FIB) lift-out technique, using an FEI Strata Dual-beam FIB-SEM at the CEMN. Electron-transparent specimens approximately 5 μm x 15 μm across were extracted from precise locations of interest identified in EBSD maps. TEM imaging of olivine for dislocation density and character and Burger's vector analysis was performed in conventional Bright Field, Selected Area Electron Diffraction, and Weak-Beam Dark Field (WBDF) modes using an FEI Technai G2 (S)TEM in the CEMN. The TEM was operated at 200 kV. Burger's vectors were determined using the conventional $\mathbf{g} = \mathbf{b} \times \mathbf{u}$ invisibility criterion.

RESULTS

EBSD LAM data for deformation and grain sizes of olivine, and LPO data for troilite and olivine, are summarized in Tables 1 and 2, respectively. Table 3 presents

TEM dislocation data for olivine. Results below are organized from progressively larger to smaller scales, including mesoscale (thin-section-wide), clast scale (local variations on a clast-sized scale), and microscale (TEM scale).

Mesoscale Deformation Features

An obvious feature of both Saint-Séverin and Elbert in thin section is their breccia texture, which is well seen in EBSD Band Contrast (BC) maps (Fig. 1). In BC images, pixel intensity is a measure of the contrast intensity of Kikuchi diffraction bands, which is related to mineral type, defect density, crystal orientation, degree of crystallinity, and other attributes (Wright et al., 2011). In the meteorites, clasts are defined by generally higher BC values than interclast, although the clasts themselves are cut by low-BC, fracture-like features, and interclast contains smaller clasts (Fig. 1). BC variation in Saint-Séverin and Elbert is probably dominated by differences in shock damage, especially differences in fracture density.

Olivine grain sizes differ between Saint-Séverin and Elbert, with fewer coarse grains in Elbert, especially in Elbert B. On average, Saint-Séverin contains ~48% more grains with d>50 μm than Elbert A, and ~285% more such grains than Elbert B (Table 1).

Shock stage OM histogram data for Saint-Séverin and Elbert olivine are shown in Fig. 2. For Saint-Séverin, a notable feature is the large variation in shock stage values for different grains, peaking at S4 but ranging broadly from S1 to S6 (Fig. 2b). The weighted shock stage of Saint-Séverin is S3.2±1.2, with a conventional shock stage of S4 based on Stöffler et al. (1991), and an undefined shock stage based on the revised criteria (which requires >50% of grains in a single shock stage) of Stöffler et al. (2018). Elbert also has a large variation in grain shock stages, peaking again at S4, but unlike Saint-Séverin

containing a large number of S6 (recrystallized) grains (Fig. 2a). For Elbert the weighted shock stage is S4.4±0.9, with a conventional shock stage of S4 (Stöffler et al., 1991) or C-S4 (Stöffler et al., 2018). The conventional shock stages for both meteorites are higher than the S2 levels estimated previously (Rubin, 2004).

Fig. 3 shows mean values for the EBSD deformation metrics $GOS_{d>50}$ and $MOS_{d>50}$ in olivine from Saint-Séverin and Elbert compared to weighted shock stage values, and compared to previously studied type 6 ordinary chondrites. For the chondrites, the average OM and EBSD deformation parameters are well correlated with one another, especially if data for Elbert are excluded (Fig. 3). Relative to the correlation established by other meteorites, the data for Elbert are displaced to higher shock stage or to lower GOS and MOS (Fig. 3). This can be explained by the presence of recrystallized grains in Elbert, which have high shock stage values but low GOS and MOS values. Large error bars in Fig. 3 for Saint-Séverin and Elbert compared to other chondrites indicate especially inhomogeneous deformation, evidenced by both EBSD and OM data.

Fig. 4 shows olivine CRA figures for 2-10° misorientations. The two meteorites have different overall CRA patterns: Saint-Séverin has a strong concentration of rotation axis directions in the <010> direction of olivine (Fig. 4a), whereas the two Elbert sections have weak but distinct concentrations in the <100> direction (Fig. 4b, c). This implies a difference between the two meteorites in the slip systems responsible for misorientations in olivine (Fig. 4d). The data correspond to a higher deformation temperature parameter for Saint-Séverin (0.80) than Elbert (identical value of 0.49 found in both A and B) (Table 1).

Values of annealing parameter (mean/median for $GOS_{d>50}$) in Saint-Séverin and Elbert are similar. Thin-section-scale annealing parameter values for Saint-Séverin, Elbert A, and Elbert B are 1.10, 1.18, and 1.13, respectively (Table 1). This indicates only small skewness in the $GOS_{d>50}$ distributions and implies relatively low degrees of post-shock annealing for both meteorites.

Fig. 5 shows pole figure plots for troilite and olivine in Saint-Séverin, Elbert A, and Elbert B. These plots imply LPOs of varying intensity in all three samples, strongest in Elbert B and weakest in Saint-Séverin (Table 2). Troilite {0001} has one principal orientation in all three sections (Fig. 5a, c, e). The Elbert A troilite pattern is more complex, with a band extending from the principal to a weaker maximum ~90° away (Fig. 5c). Olivine pole figures are more-or-less related to troilite orientations in the three samples, but in three different ways (Fig. 5, Table 2). In Saint-Séverin, olivine <100> tends to be roughly parallel and <001> roughly perpendicular to the main troilite {0001} pole (Fig. 5a, b). In Elbert A, olivine <100> tends to be within ~30° of being parallel and <010> tends to be within ~30° of being perpendicular to the main {0001} troilite pole (Fig. 5c, d). In Elbert B, olivine <100> tends to be within ~20° of perpendicular and <010> within ~20° of being parallel to the main troilite {0001} pole (Fig. 5e, f).

Clast-scale Deformation Features

Deformation features on a clast scale provide evidence for local variations and for the relationships between different types of features. Subsets for various clasts in Saint-Séverin and Elbert (Fig. 1) show differences in deformation metrics such as KAM, GOS, MOS and GROD angle but appear similar to one another in deformation temperature parameter. Annealing parameter might not be valid on the clast scale if the number of

olivine grains is too low to obtain a representative population of grains (Ruzicka and Hugo, 2018). To increase statistical validity and investigate whether there are spatial variations on a clast-interclast scale, for each sample we combined all clasts and compared this to the entire interclast region. Data for EBSD olivine deformation metrics and grain size for clasts and interclast in Saint-Séverin, Elbert A, and Elbert B are shown in Table 1.

In a given sample, clasts on average have a higher proportion of larger olivine grains, and lower values of olivine deformation metrics (KAM, GOS, MOS) than interclast areas (Table 1). For example, mean $GOS_{d>50}$ values for clast/interclast pairs in Saint-Séverin, Elbert A, and Elbert B are approximately 3.0/3.9°, 2.4/3.0°, and 3.0/3.3°, respectively (Table 1).

In contrast, there is not much difference between clast and interclast in terms of deformation temperature or annealing parameter. Deformation temperature parameter values for clast/interclast pairs in Saint-Séverin, Elbert A, and Elbert B are 0.80/0.80, 0.49/0.49, and 0.50/0.49, respectively (Table 1). Corresponding values of annealing parameter are 1.11/1.07, 1.16/1.20, and 1.10/1.18 (Table 1). Annealing parameter metric is therefore slightly higher in Saint-Séverin clast than interclast, while the reverse is true in Elbert. Whether these differences are significant is uncertain.

A localized feature visible in EBSD maps for Elbert clast regions is evidence for partial recrystallization of olivine and troilite. Recrystallized grains of olivine or troilite have low GOS, MOS, and GROD angle, and have high-angle (>15°) boundaries adjacent to deformed or other recrystallized grains, many with 120° triple grain junctions (Fig. 6a-c, f). This EBSD evidence for recrystallization is more definitive than OM evidence, but

is consistent with OM data in showing a relatively high proportion of olivine recrystallization in Elbert (Fig. 2).

In contrast to Elbert, in Saint-Séverin there is much less evidence for recrystallization of olivine and none for troilite. A notable feature in Saint-Séverin is the presence of a ~2-mm-long vein composed of multiple troilite grains in a fracture zone.

Data also show evidence for enhanced plastic deformation of troilite and olivine adjacent to fractures (Fig. 6a-e). In Elbert, some fractures in troilite and olivine appear to lead to recrystallized grains but do not cross them (Fig. 6b, c), whereas in other cases cracks pass through recrystallized and deformed grains (Fig. 6b, f).

Both Saint-Séverin and Elbert contain clasts with relict chondrules, such as might be expected for type 6 thermal metamorphism. In Clast 3A in Saint-Séverin (Fig. 1b), one such relict chondrule contains olivine more deformed than in its surroundings (Fig. 6d). The relict chondrule has olivine with mean values of $GOS_{d>50}$ (5.6±2.4°) and $MOS_{d>50}$ (24.2±9.7°) (N=14 grains) that are much higher than in Saint-Séverin overall (mean ~3.2° and ~13°, respectively, Table 1). The most prominent fracture zone in the vicinity of the chondrule bounds Clast 3A and is associated with higher values of GOS in adjacent olivine, but this fracture zone does not pass through or to the chondrule, although other fractures occur within the chondrule (Fig. 6d). For the chondrule, deformation temperature parameter (0.81) is nearly identical to that found in Saint-Séverin overall (0.80), and although annealing parameter cannot be reliably determined owing to the low number of grains, it shows no evidence for being drastically different than in Saint-Séverin overall.

Evidence for LPO was also examined on the clast scale, but on this scale there may be too few grains and data points to provide reliable fabric data, especially for troilite, which is less abundant than olivine. In Saint-Séverin, there is no clear evidence for deformation-related LPOs for either olivine or troilite in individual clast or interclast subsets of the LAM data, nor in the TAM data. Olivine fabrics are sometimes seen in clasts but appear to be related to relict chondrule textures, which could have been inherited from chondrule formation.

In contrast to Saint-Séverin, the evidence for Elbert suggests local variations in olivine and troilite LPOs that could be related to deformation. In Elbert A, one TAM (Clast 1, Site 12) was acquired (Fig. 6c). In this map, troilite and olivine have apparent LPOs with the same crystallography relationship as for the LAM dataset in Elbert A (i.e., <100>olivine quasi-parallel to <0001>troilite, Table 2), but troilite and olivine are more closely aligned. They are both ~90° different than the LAM LPOs, however. In the Elbert A Clast 1 and LAM datasets there are a similar number of troilite grains (Ng=899 for Clast 1, Ng=1121 for the LAM).

Two TAMs were acquired for Elbert B. In Elbert B Clast 6 (Site 2), olivine LPO is weak or non-existent, but $\{0001\}_{troilite}$ has an LPO which is ~45° different than the LAM dataset, with a comparable number of troilite grains (N_g=996 for Clast 6, N_g=2120 for LAM). In Elbert B Clast 1 (Site 1), there are only N_g=338 grains for troilite, which has an {0001} LPO ~90° different than the LAM dataset. But Elbert B Clast 1 olivine has the same LPO relationship to troilite in this clast as in Elbert A (LAM and Elbert A Clast 1) (i.e., $<100>_{olivine}$ quasi-parallel to $<0001>_{troilite}$), despite being different than the crystallography relationship shown for the Elbert B LAM dataset (Table 2).

The presence of troilite LPOs in the Elbert TAMs that have orientation relationships to olivine similar to those found in LAM datasets and/or with a large number of grains for troilite suggests that orientation differences from the global patterns could be real. These local orientation differences are large (~45-90°).

Microscale Deformation Features

Olivine TEM data for Elbert and Saint-Séverin are summarized in Table 3, and TEM images showing representative olivine microstructures are shown in Fig. 7 (Elbert and Saint-Séverin clasts) and Fig. 8 (Saint-Séverin interclast).

In Elbert, TEM evidence is in close accordance with EBSD and OM results. WBDF images reveal a dislocation structure primarily of ***c***-type (**b**=[001]) dislocations with long, straight screw segments and relatively short edge segments (Fig. 7a-c). ***a***-type (**b**=[100]) dislocations are rare, comprising <5% of the total number identified. This type of microstructure is commonly associated with shock (Ashworth and Barber, 1975; Sears et al., 1984; Leroux, 2001; Langenhorst, 2002) and would be expected to produce crystal rotations around <100>, as observed (Fig. 4b, c). In some areas the non-screw segments are curved (Fig. 7a), whereas in others they are straight and associated with two distinct orientations (Fig. 7b). The latter configuration is consistent with ***c***-type slip constrained to {hk0} planes. Both configurations indicate slightly elevated shock temperatures. The only subgrain boundaries found in Elbert olivine are composed of the kink band type, composed of dislocation pileups or tangles which can be produced during deformation. An example is the subplanar array of ***a***-type dislocations in Figure 7c. This array cuts through a number of ***c***-type dislocations, creating dislocation jogs. No picket-fence low angle subgrain boundaries, such as might be expected for significant recovery during

annealing (Trepman et al., 2013; Ruzicka et al., 2015; Ruzicka and Hugo, 2018), were observed. This is in accordance with relatively low values of EBSD annealing parameter in Elbert which are only slightly greater than 1 (Table 1), suggestive of little annealing (Ruzicka and Hugo, 2018). Dislocation densities in Elbert range from ~$1.6x10^9$ to $1.3x10^{10}$ cm^{-2} (Table 3), consistent with shock stage S4 or higher (Ruzicka and Hugo, 2018).

For Saint-Séverin clast olivine, TEM data are again mostly consistent with EBSD and OM data. TEM imaging reveals a predominance of curved and looped ***c***-type dislocations (Fig. 7d, e, f). ***a***-type dislocations comprise <5% of the total number identified. Dislocation densities range from ~$1.6x10^7$ to $4.2x10^9$ cm^{-2} (Table 3). This is consistent with the common S2-S4 shock values observed with OM (Fig. 2). No picket-fence low angle subgrain boundaries (annealing type) were found, though high-density dislocation tangles creating slight misorientations are common (Fig. 7e).

The predominant curved and looped dislocation microstructure in Saint-Séverin clast olivine suggests that this material was warm enough during deformation that dislocations could deviate from their low energy, straight-line configurations (Poirier, 1995; Ruzicka and Hugo, 2018), but the lack of picket-fence subgrain boundaries suggests that there was little post-deformation annealing. This is consistent with Saint-Séverin CRA data (Fig. 4) and high values of EBSD deformation temperature parameter (Table 1).

In one clast area of Saint-Séverin a tangle of dislocations are associated with metal-sulfide inclusions that form a band within olivine (Fig. 7f). These inclusions appear to correspond to the “blackening” inclusions studied by Leroux et al. (1996). In this area

at least, the inclusions do not occur at a grain boundary or along an identifiable fracture and occur within olivine that is weakly deformed.

TEM data were obtained from eight interclast areas in Saint-Séverin (Table 3, Fig. 8). This includes one area (FIB 9) that was examined by high-resolution EBSD mapping prior to FIB extraction, providing good context information (Fig. 8c-h). Interclast olivine is found by TEM to be highly deformed, with many curved free dislocations and multiple subgrain boundaries composed of dislocation tangles (Fig. 8a, b, g, h). The dislocation density of interclast olivine was measured as ~2.6×10^9 to 1.0×10^{10} cm^{-2} (Table 3). This overlaps but tends to be higher than what is found in Saint-Séverin clast areas, indicating generally greater deformation. The high degree of TEM-scale deformation of olivine in interclast compared to clast areas in Saint-Séverin is consistent with the high values of EBSD deformation metrics (GOS, MOS, GROD angle—Fig. 8c, KAM—Fig. 8d) for interclast compared to clast in this meteorite (Table 1).

Both ***a***-type and ***c***-type dislocations were found in the Saint-Séverin interclast area. WBDF images of the FIB 9 specimen show that ***a***-type dislocations are arranged in sub-planar arrays forming misorientation boundaries, with ***c***-type dislocations being more randomly distributed (Fig. 8g, h). The proportion of ***a***-type dislocations in interclast is significantly higher than in Saint-Séverin clast areas (Table 3).

The relatively large number of ***a***-type dislocations in interclast olivine is unambiguous evidence for high temperature deformation (see Ruzicka et al., 2015; Ruzicka and Hugo, 2018; and references therein), which was evidently higher in interclast than in clasts. CRA plots for olivine in this interclast compared to adjacent clast show evidence for fewer rotations around the “low temperature” <100> axis for interclast

(Fig. 8f), consistent with a higher deformation temperature in interclast. However, the difference is slight and not much reflected in deformation temperature parameter, which has nearly identical values for interclast (0.81) and adjacent clast (0.80). These values are similar to those found throughout overall clast and interclast in Saint-Séverin (Table 1). Thus, TEM more clearly than EBSD indicates local variations in deformation temperature in Saint-Séverin.

DISCUSSION

Comparison Between Saint-Séverin, Elbert, and Other Chondrites

There are similarities and differences in the deformation features of Saint-Séverin and Elbert. A prominent similarity is the obvious breccia texture of both meteorites, which implies both meteorites were affected by brittle deformation. This brittle deformation was associated with localized plastic deformation, as shown by increased KAM, GOS, and MOS values in olivine and troilite near fractures. Increased fracture density and associated plastic deformation probably accounts for higher levels of deformation in interclast compared to clast areas in both meteorites.

Another important similarity is that the amount of post-shock annealing was low in both meteorites. Misorientation boundaries in olivine observed with TEM are composed of tangles and parallel sets of dislocations that are better explained as having been produced by deformation than by annealing. In Fig. 7c, for example, an ***a***-type dislocation array cutting through ***c***-type dislocations is best explained as a pileup of gliding dislocations, as the observed dislocation jogs could not be produced by recovery and annealing processes. Similarly, dislocation tangles visible in Figure 7e are highly curved and looped, indicating that they have not experienced a significant recovery

process, which would produce straight dislocations with minimum line energy. An exception to the general lack of recovery features is the well-developed arrays of interlocking ***c-*** and ***a-***type dislocations visible in Fig. 8g and 8h. These low angle sub-boundaries clearly experienced some recovery which, given the lack of similar features in the clasts, is best explained by a localized thermal excursion. The general lack of TEM-scale annealing features is consistent with low skewness in $GOS_{d>50}$ distributions for olivine in both meteorites, corresponding to low values of EBSD annealing parameter.

The two chondrites differ in that recrystallization of olivine was much more prevalent in Elbert, as evidenced by both OM and EBSD data. This recrystallization implies more intense deformation of Elbert, sufficient to increase weighted shock stages, remove plastic deformation, and lower mean $GOS_{d>50}$ and $MOS_{d>50}$ values. More intense deformation of Elbert clasts than Saint-Séverin clasts is consistent with mostly higher dislocation densities and shock stages in olivine from Elbert (Table 3, Fig. 2).

Another significant difference is that deformation temperatures were higher in Saint-Séverin than in Elbert. TEM dislocation data for olivine show more evidence for elevated deformation temperature in Saint-Séverin, and EBSD deformation temperature parameter is much higher for Saint-Séverin. This is despite evidence for rather intense deformation of Elbert, which should have produced more dynamic heating in Elbert if all else was equal. The high deformation temperatures for Saint-Séverin must instead reflect high ambient temperature at the time of deformation.

Compared to meteorites previously studied by Ruzicka et al. (2015) and Ruzicka and Hugo (2018), the overall deformation levels in Saint-Séverin and Elbert are similar to that expected for an S4 chondrite such as Leedey and Bruderheim, based on olivine OM

shock stage data (Fig. 2), GOS-MOS systematics (Fig. 3), and dislocation densities (Table 3), though Saint-Séverin has some less deformed olivine. Elbert is the first good meteorite example studied with EBSD to show partial recrystallization of olivine (in addition to matrix clasts in the melt breccia MIL 07273; Ruzicka et al., 2017), and both Saint-Séverin and Elbert have unusually distinct evidence for brecciation.

To first approximation, Elbert resembles other high-shock (S4-S5) chondrites previously studied such as Leedey, Bruderheim, and Morrow County with regard to low values of deformation temperature and annealing parameter (Fig. 9) and the presence of recrystallized troilite (Ruzicka and Hugo, 2018). Among the previous meteorites, Elbert probably most closely resembles the strongly shocked (S5) Morrow County in containing olivine with some ***a***-type dislocations (Ruzicka et al., 2015) and in CRA distributions implying significant [001]{hk0} slip (Ruzicka and Hugo, 2018). However, EBSD deformation temperature parameter and annealing parameter are slightly higher in Elbert compared to the other high-shock chondrites, including Morrow County (Fig. 9). Elevated temperature can be explained by more dynamic heating during more intense shock, and higher annealing parameter could be caused by Elbert cooling in a larger, hotter impact deposit than other meteorites of this class. Morrow County may have been heated briefly to ~700-800° C (Ruzicka and Hugo, 2018), so Elbert may have been heated briefly to ≥700-800° C.

In Saint-Séverin the temperature of deformation was high but the extent of post-shock annealing was low, unlike all other type 6 chondrites examined to date. This is reflected both by EBSD evidence for high deformation temperature parameter and low annealing parameter (Fig. 9), as well as by TEM evidence for dislocations that do not

conform to a low energy configuration and a lack of picket-fence subgrain boundaries. The closest analogue to Saint-Séverin is the melt clast in MIL 99301 (LL6), which also shows evidence for being hot-deformed and little-annealed (Fig. 9). But EBSD evidence implies that the deformation temperature could have been even higher in Saint-Séverin than in the MIL 99301 melt clast (Fig. 9). Next most similar to Saint-Séverin in temperature-annealing combination is Park (L6), which could have been similarly hot-deformed, but which was more annealed (Fig. 9). Park also differs in containing recrystallized troilite and weakly deformed olivine, a signature of elevated pre-shock temperature (Schmitt, 2000), whereas recrystallization was not observed in Saint-Séverin troilite. Elevated pre-shock temperature is compatible for Saint-Séverin, however, if troilite was melted instead of recrystallized (Schmitt, 2000; Ruzicka and Hugo, 2018). Such melting is suggested by the ~2-mm-long troilite vein in Saint-Séverin.

Temperature during deformation in Saint-Séverin can be estimated by comparison to Park and the MIL 99301 melt clast. Given that deformation temperatures of Park and the MIL 99301 melt clast were estimated as ~800-1000 °C and ≥1100 °C, respectively (Ruzicka and Hugo, 2018), EBSD temperature metric values imply that Saint-Séverin was deformed at temperatures >800-1100 °C. Temperatures were probably high enough to partially melt sulfide and metal during impact, consistent with the blackening inclusions observed for this meteorite (Leroux et al., 1996; Fig. 7f).

Multistage Deformation and Overprinting

Evidence for multiple impact effects in both Elbert and Saint-Séverin can be evaluated by considering various petrographic and crystallographic features. Evidence to consider includes LPO data, cross-cutting relationships between different deformation

features, and spatial variability in deformation extent, deformation temperature, and annealing extent.

Most LPO data do not strongly point to either multiple impacts, or to one impact. The presence of global LPOs for troilite in both Saint-Séverin and Elbert samples implies one dominant compression direction during the formation of the final breccia texture. These are related to olivine LPO directions. However, in Elbert at least, differences in troilite and olivine LPOs between different clasts and the global LPO orientation suggests either 1) rotation of clasts, or 2) incomplete realignment of pre-existing LPO patterns during the last compressive episode. Both possibilities allow one impact or several.

More significant is the LPO pattern for troilite in Elbert A, with a primary {0001} pole and band extending to a weaker maximum (Fig. 5c). This resembles that of troilite in Park, which was interpreted as indicative of a second impact partially reorienting troilite (Ruzicka and Hugo, 2018). This suggests multiple impacts for Elbert A and constitutes significant evidence that Elbert was shocked at least twice.

In Elbert, fractures cut recrystallized grains, suggesting some came late after earlier deformation. This provides further evidence that the meteorite was affected by at least two impacts. But some fractures lead to, but do not cross, recrystallized grains. This could indicate that fractures were more likely to propagate through deformed but unrecrystallized olivine than through recrystallized olivine. The data for Elbert thus can be explained by a second impact involving modest fracturing and fabric development.

The intensity of deformation was not uniform throughout Saint-Séverin and Elbert. In principle, this can be explained either by inhomogeneous deformation during one impact event or by incorporation of components with different deformation extent

during breccia formation. Inhomogeneous deformation during one impact event could explain higher deformation in interclast regions, if fracturing promoted more plastic deformation, for which there is evidence. Similarly, local recrystallization of olivine in Elbert was probably caused by inhomogeneous deformation as a result of variations in chondrite texture and fracture locations, given that recrystallized areas often occur near fractures or clast edges. The best evidence for incorporation of a component that may have been shocked before breccia formation is the relict chondrule in Clast 3A in Saint-Séverin, which is more deformed than its surroundings. In this case the enhanced deformation of the chondrule cannot be easily explained by localized deformation along a fracture zone that led to brecciation. However, it might still be possible for stress waves to become focused on this chondrule owing to variations in texture (e.g., the chondrule has coarser grains than in its surroundings, as well as a pyroxene rim), so inhomogeneous deformation during one impact event cannot be ruled out.

In contrast to deformation intensity, spatial variations in deformation temperature and annealing extent appear to be modest. One interclast area in Saint-Séverin does show good TEM evidence for both deformation under higher temperature conditions and limited dislocation recovery. But only small variations in annealing parameter and temperature parameter occur between clast and interclast, and between chondrule 3A and its surroundings. These similarities do not provide any evidence for multiple impact events. Instead, they imply control by a single event that was not overprinted by later events.

We therefore suggest that deformation temperature and annealing signatures are established by the last dominant impact. The temperature signatures depend on rotation

axes of misorientations, which because of work hardening, may be difficult to reset unless subsequent shocks are stronger than prior events. Further, annealing signatures depend on having sufficient heat and time to result in the migration of dislocations to subgrain or grain boundaries in olivine. Dislocation recovery kinetics in olivine are slow and comparable to a slow-diffusing species such as oxygen (Farla et al. 2011). Thus, significant annealing will be possible only for a major thermal event, either by a strong shock or an already warm target at the time of impact, followed by burial conditions that provide slow cooling. Thus, subsequent impacts of weak intensity will be generally incapable of changing either the deformation temperature or annealing signatures, although annealing condition could be changed by even a weak impact on a hot parent body if it redistributed material to a different thermal environment.

Thus, both Saint-Séverin and Elbert could be recording one dominant impact that produced inhomogeneous deformation and breccia textures, although later, weak impacts are fully compatible with the observations. Data for Elbert can be explained by a model in which pre-existing cold rock was crushed, plastically deformed, and heated briefly during one intense shock event. Inhomogeneous shock effects resulted in localized olivine recrystallization and more deformation in interclast regions. Later shock events may have occurred to result in clast rotation, partial reorientation of troilite by plastic deformation (Elbert A), and some fracturing of recrystallized grains.

Data for Saint-Séverin can be explained by a model in which pre-existing warm rock was crushed, plastically deformed, and cooled more strongly afterwards. Enhanced temperatures may have been achieved in some interclast regions of Saint-Séverin, possibly as a result of frictional heating in fracture zones (Spray, 1992; van de Bogert et

al., 2003) or heating caused by collapse of pore spaces (Scott et al., 1992; Nakamura et al. 1995; Rubin, 2004; Bland et al., 2014; Davison et al., 2016) in crushed areas. If one event was involved to make clasts and interclast in Saint-Séverin, this event was not so hot as to prevent brittle deformation. A later shock event may have resulted in additional fracturing and plastic deformation that led to establishment of weak troilite LPO and flattening of metal grains.

Shock History of Saint-Séverin

Inferences made here for Saint-Séverin can be reconciled with previous work. In particular, results support modest deformation occurring during thermal metamorphism as first suggested by Ashworth and Barber (1977). The inferred high-temperature deformation and limited post-shock annealing of Saint-Séverin also fit with the model of Ganguly et al. (2016), whereby Saint-Séverin was shock-excavated from a warm parent body that was being thermally metamorphosed, then cooled much more rapidly, probably by being brought to a near-surface, cooler region of the parent body. The rapid cooling we infer was probably relevant at temperatures >450 °C, the estimated transition temperature to slow cooling inferred for Saint-Séverin (Ganguly et al., 2016) needed to account for metallographic and other data (Willis et al., 1983; Leroux et al., 2000; Ganguly et al., 2016).

At first blush it seems that some of our results are contrary to the interpretations of Leroux et al. (1996). The annealing episode following an early shock interpreted by Leroux et al. (1996) could explain the presence of metal-sulfide inclusion “blackening” trails, as found by those researchers and by us, if these were injected along fractures that became healed. In this case, dislocation tangles found around such inclusions (Fig. 7f)

could represent the vestiges of annealing of a pre-existing crack or deformation zone. However, protracted annealing in a separate episode following shock is inconsistent with a lack of subgrain boundaries attributable to annealing and for the distribution of GOS values that implies limited annealing following shock. Further, unlike Leroux et al. (1996), we find no TEM evidence for late cold shock. We found some straight dislocations in screw configuration, similar to areas found by Leroux et al. (1996), but these are rare compared to widespread curved dislocations and loops, and thus do not provide significant evidence for cold shock. Even so, a late (possibly cold) shock event is consistent with different features in Saint-Séverin, including: 1) evidence for late fracturing evident with EBSD; 2) the dislocation tangles in olivine around inclusions, if these served as dislocation nucleation points; 3) the weak global LPO of troilite found in this study, consistent with a late weak compaction event; and 4) the modest shape preferred orientation of metal, consistent with a late weak compaction event (Friedrich et al., 2017).

Given these observations and constraints, we suggest that *three* impacts were important for Saint-Séverin. Impact #1 could have occurred while the meteorite source area was warm; this impact could have injected liquefied metal-sulfide into fractures within silicates. If the source region remained warm, this could have allowed annealing and healing of fracture zones to leave metal-sulfide inclusion trails within silicates. Impact #2 could have been the major shock event, also occurring while Saint-Séverin was warm. This impact would have resulted in partial excavation of Saint-Séverin to a cooler portion of the parent body, explaining signatures for high-temperature deformation and minimal annealing following such deformation. Most of the brecciation evident would

have occurred during Impact #2, producing interclast areas by comminution. Finally, Impact #3 could have resulted in some fracturing, minor plastic deformation, and the modest preferred orientation effects for troilite and metal. This three-impact scenario is consistent with most available data for Saint-Séverin.

Impact and Metamorphic Processes on the LL Chondrite Asteroid

Saint-Séverin and Elbert provide a contrasting picture of the LL chondrite parent body (we assume one, but there could have been more) at what were probably different times. For Saint-Séverin, the source region in the parent body was shocked while it was warm. Temperatures during deformation were probably similar to what was needed for type 6 thermal metamorphism (Ruzicka and Hugo, 2018). High ambient temperature at the time of deformation could have been caused by impact on an internally heated parent body (Harrison and Grimm, 2010; Ciesla et al., 2013; Scott et al., 2014) warmed by short-lived radionuclide decay (e.g., ^{26}Al) (Grimm and McSween, 1993; Ghosh et al., 2005), or by impact in a localized hot impact deposit on the parent body (Davison et al., 2012). The two different Ar plateau age dates of Saint-Séverin, ~4.42 Ga for a dark portion and ~4.38 Ga for a light portion (Hohenberg et al., 1981), implies two shock events. In hand specimens of Saint-Séverin prepared for study, darker clasts are set in a lighter interclast. Thus, we adopt an age of ~4.42 Ga for the clasts and ~4.38 Ga for the interclast, which we interpret as having formed by the comminution of clasts.

There are two possibilities for which of these two shock events represent the “last major impact” as recorded by EBSD and TEM. If the 4.42 Ga age of the clasts corresponds to the last major impact, and the clasts were deformed while the source was already hot as suggested here, then the source area must have been warm around that

time. Given that Saint-Séverin could have cooled rapidly after impact (Ganguly et al., 2016), this would not leave much of a time interval between the impact and the Ar closure age, implying impact on a warm body shortly before 4.42 Ga ago. The younger age of interclast might indicate a later, weaker shock event not able to reset deformation temperature signatures of olivine but able to result in some Ar degassing. However, this scenario has difficulty explaining all of the deformation features in Saint-Séverin. In particular, with this model it is difficult to reconcile the lack of fractures associated with blackening inclusions and the good evidence for minimal annealing following the major impact.

Alternatively, and more consistent with the scenario presented in the previous section, the second impact may have been the last major impact. The interclast may have formed by a significant impact event at ~4.38 Ga (or shortly before), while the parent body was still hot, accounting for the elevated temperature signature of Saint-Séverin components and degassing at that time. The earlier age of clasts could reflect an early impact event less strong than the later one, but which nonetheless introduced metal and sulfide blackening inclusions, followed by annealing to heal fractures. The second impact was relatively strong, but not sufficiently strong to appreciably recrystallize olivine or troilite, although troilite may have been melted. In this scenario, the Saint-Séverin parent body source area probably was warm between ~4.42-4.38 Ga ago. If caused by short-lived radionuclide heat, this heat source was able to keep the LL parent body warm at least this late. However, the second impact may have occurred in a source area that was warm partly as a result of impact heating associated with the first impact. In this case, both radiogenic and impact heating may have contributed to warm conditions during the

deformation of Saint-Séverin. Another later, weak impact, not recorded by the Ar data, may have resulted in additional, minor shock effects, including fracturing and formation of weak crystal fabrics.

In either case, as noted above, the data for Saint-Séverin are best explained by excavation of hot material to a near-surface cool environment following the last major impact, resulting in little to no post-shock annealing of olivine. This implies significant collisional scrambling of the LL parent body at ~4.4 Ga ago. Rapid cooling after the major impact helped preserve the distinct breccia texture of the rock.

In contrast, Elbert was shocked while the source region on the parent body was cold, probably long after thermal metamorphism was complete. No Ar age dates for Elbert are available. But Elbert was probably shocked more recently than 4.4 Ga ago when short-lived radionuclide heat sources were less potent, and when the only heat on or within asteroidal parent bodies was that produced by impact. Elbert was strongly shocked, and such strong shock could have caused some dynamic heating. Both strong deformation and dynamic heat promoted recrystallization and possibly a small amount of post-shock annealing. These conditions imply that Elbert formed in a hot impact deposit. But the deposit was not so extensive so to keep rock warm for very long and result in more significant annealing. Thus, the hot deposit must have been localized. As with Saint-Séverin, the breccia texture of Elbert was preserved distinctly because of relatively rapid cooling after formation of the hot deposit.

For both Elbert and Saint-Séverin, late, weak impacts are inferred to have resulted in fracturing and modest plastic deformation. One or more of these impact events could

have been associated with the ejection of the Elbert and Saint-Séverin source bodies from the parent body.

CONCLUSION

1. A detailed optical, EBSD, and TEM study of the Saint-Séverin and Elbert LL6 chondrites on various scales suggests some similarities and differences between the two meteorites. Both are shock stage S4 according to the scale of Stöffler et al. (1991) and show distinct breccia textures, but Elbert was more intensely shocked overall with partial recrystallization of both olivine and troilite.

2. Elbert was shocked while cold and could have experienced significant dynamic heating and a small amount of annealing in a hot impact deposit. One or more later, weaker impact events may have resulted in modest late deformation.

3. Saint-Séverin experienced a major impact event while the parent body source region was still warm, in a possibly disruptive event for the LL parent body ~4.4 Ga ago. Heat may have been contributed both by radioactive heating and a previous impact. In any case, the meteorite source region was excavated to a cooler, near-surface region of the parent body. There is evidence in Saint-Séverin for yet another later impact event.

4. TEM provides more detailed information about spatial variations in deformation temperatures and on the nature of subgrain boundaries than EBSD, whereas EBSD provides better information on larger-scale deformation features and their spatial relationships.

5. EBSD deformation temperature and annealing signatures appear to be controlled by the last major deformation event.

Acknowledgments— This study was supported by NASA grant NNX14AF39G (PI AER), Subaward No. 2090 GRA940 (PI AMR, Co-I RCH). The authors dedicate this paper to the memory of Christine Floss who will be greatly missed. Constructive comments by two anonymous reviewers and editorial handling by Dr. Larry Nittler are appreciated.

REFERENCES

Ashworth J.R. and Barber D.J. 1975. Electron petrography of shock-deformed olivine in stony meteorites. *Earth and Planetary Science Letters* 27: 43-50.

Ashworth J.R. and Barber D.J. 1977. Electron microscopy of some stony meteorites. *Phil. Trans. R. Soc. Lond. A*. 286(1336): 493-506.

Bischoff A., Schleiting M., Wieler R. and Patzek M., 2018a. Brecciation among 2280 ordinary chondrites—Constraints on the evolution of their parent bodies. *Geochimica et Comsochimica Acta* 238: 516-541.

Bischoff A., Schleiting M. and Patzek M., 2018b. Shock stage distribution of 2280 ordinary chondrites—Can bulk chondrites with a shock stage of S6 exist as individual rocks? *Meteoritics & Planetary Science*. https://onlinelibrary.wiley.com/doi/pdf/10.1111/maps.13208

Blackburn T., Alexander C.M.D., Carlson R. and Elkins-Tanton L.T., 2017. The accretion and impact history of the ordinary chondrite parent bodies. *Geochimica et Cosmochimica Acta* 200: 201-217.

Bland P.A., Collins G.S., Davison T.M., Abreu N.M., Ciesla F.J., Muxworthy A.R. and Moore J., 2014. Pressure–temperature evolution of primordial solar system solids during impact-induced compaction. *Nature communications* 5: 5451-5463.

Ciesla F.J., Davison T.M., Collins G.S. and O'Brien D.P., 2013. Thermal consequences of impacts in the early solar system. *Meteoritics & Planetary Science* 48(12):.2559-2576.

Davison T.M., Ciesla F.J. and Collins G.S. 2012. Post-impact thermal evolution of porous planetesimals. *Geochimica et Cosmochimica Acta* 95:.252-269.

Davison T.M., Collins G.S. and Bland P.A., 2016. Mesoscale modeling of impact compaction of primitive solar system solids. *The Astrophysical Journal* 821(1): 68-85.

Farla R.J.M., Kokkonen H., Gerald J.F., Barnhoorn A., Faul U.H. and Jackson I., 2011. Dislocation recovery in fine-grained polycrystalline olivine. *Physics and Chemistry of Minerals* 38(5): 363-377.

Friedrich J.M., Ruzicka A., Rivers M.L., Ebel D.S., Thostenson J.O. and Rudolph R.A. 2013. Metal veins in the Kernouve (H6 S1) chondrite: Evidence for pre- or syn-metamorphic shear deformation. *Geochimica et Cosmochimica Acta* 116: 71-83.

Friedrich J.M., Rubin A.E., Beard S.P., Swindle T.D., Isachsen C.E., Rivers M.L. and Macke R.J. 2014. Ancient porosity preserved in ordinary chondrites: Examining shock and compaction on young asteroids. *Meteoritics & Planetary Science* 49 (7): 1214-1231.

Friedrich J.M., Ruzicka A., Macke R.J., Thostenson J.O., Rudolph R.A., Rivers M.L. and Ebel D.S. 2017. Relationships among physical properties as indicators of high temperature deformation or post-shock thermal annealing in ordinary chondrites. *Geochimica et Cosmochimica Acta* 203: 157-174.

Ganguly J., Tirone M., Chakraborty S. and Domanik K. 2013. H-chondrite parent asteroid: A multistage cooling, fragmentation and re-accretion history constrained by thermometric studies, diffusion kinetic modeling and geochronological data. *Geochimica et Cosmochimica Acta* 105: 206-220.

Ganguly J., Tirone M. and Domanik K. 2016. Cooling rates of LL, L and H chondrites and constraints on the duration of peak thermal conditions: Diffusion kinetic modeling and implications for fragmentation of asteroids and impact resetting of petrologic types. *Geochimica et Cosmochimica Acta* 192: 135-148.

Ghosh A., Weidenschilling S.J., McSween Jr, H.Y. and Rubin A. 2006. Asteroidal heating and thermal stratification of the asteroid belt. In *Meteorites and the Early Solar System II* (eds. D.S. Lauretta and H.Y. McSween, Jr.), pp.555-566. University of Arizona Press: Tucson.

Grimm, R.E. and McSween Jr, H.Y. 1993. Heliocentric zoning of the asteroid belt by aluminum-26 heating. *Science* 259: 653-655.

Harrison K.P. and Grimm R.E. 2010. Thermal constraints on the early history of the H-chondrite parent body reconsidered. *Geochimica et Cosmochimica Acta* 74(18): 5410-5423.

Hohenberg C.M., Hudson B., Kennedy B.M. and Podosek F.A. 1981. Noble gas retention chronologies for the St Severin meteorite. *Geochimica et Cosmochimica Acta* 45(4): 535-546.

Jamsja N. and Ruzicka A. 2010. Shock and thermal history of Northwest Africa 4859, an annealed impact-melt breccia of LL chondrite parentage containing unusual igneous features and pentlandite. *Meteoritics & Planetary Science* 45(5): 828-849.

Keil K 1982. Composition and origin of chondritic breccias. In *Workshop on Lunar Breccias and Soils and their Meteoritic Analogs* (eds. G. J. Taylor and L. L. Wilkening), pp. 65-83. Lunar and Planetary Institute, LPI Technical Report 82-02.

Langenhorst F. 2002. Shock metamorphism of some minerals: Basic introduction and microstructural observations. Bulletin of the Czech Geological Survey 77 (4): 265-282.

Leroux H. 2001. Microstructural shock signatures of major minerals in meteorites. European Journal of Mineralogy 13: 253-272.

Leroux H., Doukhan J.C. and Guyot F. 1996. An analytical electron microscopy (AEM) investigation of opaque inclusions in some type 6 ordinary chondrites. *Meteoritics & Planetary Science* 31 (6): 767-776.

Nakamura T., Tomeoka K., Sekine T. and Takeda H. 1995. Impact-induced chondrule flattening in the Allende CV3 carbonaceous chondrite: Shock experiments. *Meteoritics* 30 (3): 344-347.

Poirier J. P. 1995. Plastic Rheology of Crystals. In *Mineral Physics & Crystallography: A Handbook of Physical Constants, Volume 2*, pp. 237–247. American Geophysical Union (AGU).

Rubin A.E. 2004. Postshock annealing and postannealing shock in equilibrated ordinary chondrites: Implications for the thermal and shock histories of chondritic asteroids 1. *Geochimica et Cosmochimica Acta* 68 (3): 673-689.

Rubin A.E. and Jones R.H. 2003. Spade: An H chondrite impact-melt breccia that experienced post-shock annealing. *Meteoritics & Planetary Science* 38 (10): 1507-1520.

Ruzicka A.M. and Hugo R.C. 2018. Electron Backscatter Diffraction (EBSD) study of seven heavily metamorphosed chondrites: Deformation systematics and variations in pre-shock temperature and post-shock annealing. *Geochimica et Cosmochimica Acta* 234: 115-147.

Ruzicka A., Hugo R., and Hutson M. 2015. Deformation and thermal histories of ordinary chondrites: Evidence for post-deformation annealing and syn-metamorphic shock. *Geochimica et Cosmochimica Acta* 163: 219-233.

Ruzicka A., Hutson M., Friedrich J.M., Rivers M.L., Weisberg M.K., Ebel D.S., Ziegler K., Rumble D. and Dolan A.A. 2017. Petrogenesis of Miller Range 07273, a new type of anomalous melt breccia: Implications for impact effects on the H chondrite asteroid. *Meteoritics & Planetary Science* 52: 1963-1990.

Schmitt R.T. 2000. Shock experiments with the H6 chondrite Kernouvé: Pressure calibration of microscopic shock effects. *Meteoritics & Planetary Science* 35(3): 545-560.

Schmitt R.T. and Stöffler D. 1995. Experimental data in support of the 1991 shock classification of chondrites. *Meteoritics* 30: 574-575.

Scott E.R., Keil K. and Stöffler D. 1992. Shock metamorphism of carbonaceous chondrites. *Geochimica et Cosmochimica Acta* 56(12): 4281-4293.

Scott E.R., Krot T.V., Goldstein J.I. and Wakita S. 2014. Thermal and impact history of the H chondrite parent asteroid during metamorphism: Constraints from metallic Fe–Ni. *Geochimica et Cosmochimica Acta* 136: 13-37.

Sears D.W., Ashworth J.R., Broadbent C.P. and Bevan A.W.R. 1984. Studies of an artificially shock-loaded H group chondrite. *Geochimica et Cosmochimica Acta* 48 (2): 343-360.

Spray J.G. 1992. A physical basis for the frictional melting of some rock-forming minerals. *Tectonophysics* 204: 205-211.

Stöffler D., Keil K. and Scott E.R.D. 1991. Shock metamorphism of ordinary chondrites. *Geochimica et Cosmochimica Acta* 55 (12): 3845-3867.

Stöffler D., Hamann C. and Metzler K. 2018. Shock metamorphism of planetary silicate rocks and sediments: Proposal for an updated classification system. *Meteoritics & Planetary Science* 53(1): 5-49.

Trepmann C. A., Renner J., and Druiventak A. 2013. Experimental deformation and recrystallization of olivine-processes and timescales of damage healing during postseismic relaxation at mantle depths. *Solid Earth* 4: 423–450.

van de Bogert C.H., Schultz P.H. and Spray J.G. 2003. Impact-induced frictional melting in ordinary chondrites: a mechanism for deformation, darkening, and vein formation. *Meteoritics & Planetary Science* 38 (10): 1521-1531.

Willis J. and Goldstein J.I., 1983. A three-dimensional study of metal grains in equilibrated, ordinary chondrites. *Journal of Geophysical Research: Solid Earth* 88: B287-B292.

Wright S.I., Nowell M.M. and Field D.P. 2011. A review of strain analysis using electron backscatter diffraction. *Microscopy and Microanalysis* 17(3): 316-329.

Table 1. Deformation and grain size data for olivine in Saint-Séverin (St. Séverin) and Elbert based on EBSD Large Area Maps (LAMs). Elbert "A" and "B" refer to different pieces of Elbert.

	St. Séverin all	St. Séverin Clasts	St. Séverin Interclast	Elbert A All	Elbert A Clasts	Elbert A Interclast	Elbert B all	Elbert B Clasts	Elbert B Interclast
N_g[1]	47513	32974	14539	20907	14243	7058	19888	9502	10776
N_p[2]	2097227	1563922	533305	796275	542709	253566	1387314	758972	628342
d range (μm)[3]	10.1-469	10.1-469	10.1-327	10.1-425	10.1-425	10.1-276	5.0-367	5.0-367	5.0-220
$d_{50/10}$ (%)[4]	4.20	4.87	2.68	2.83	3.16	2.43	1.47	2.01	1.15
KAM (°)[5]	2.09	1.87	2.78	1.96	1.75	2.44	1.56	1.36	1.83
$GOS_{all\ d}$ (°)[6]	2.64 (1.76)	2.34 (1.64)	3.29 (1.84)	2.04 (1.42)	1.81 (1.28)	2.54 (1.56)	2.02 (1.40)	1.69 (1.23)	2.33 (1.48)
$GOS_{d>50}$ (°)[7]	3.17 (1.67)	2.99 (1.62)	3.89 (1.68)	2.55 (1.46)	2.40 (1.39)	3.03 (1.54)	3.09 (1.47)	2.99 (1.36)	3.27 (1.60)
$GOS_{d<50}$ (°)[8]	2.61 (1.76)	2.31 (1.64)	3.28 (1.84)	2.02 (1.41)	1.79 (1.27)	2.53 (1.56)	2.00 (1.39)	1.66 (1.21)	2.32 (1.48)
$MOS_{d>50}$ (°)[9]	12.8 (6.0)	12.3 (6.0)	14.8 (5.5)	9.80 (5.18)	9.22 (4.89)	11.7 (5.4)	13.0 (5.4)	12.7 (5.3)	13.9 (5.6)
$GOS_{d>50}$ mean / median[10]	1.10	1.11	1.07	1.18	1.16	1.20	1.13	1.10	1.18
$f_{<010>+<001>}$ (2-10°)[11]	0.80	0.80	0.80	0.49	0.49	0.49	0.49	0.50	0.49
MAD (°)[12]	0.73	0.72	0.76	0.84	0.83	0.87	0.86	0.84	0.89

[1] Number of olivine grains. [2] Number of olivine pixels. [3] Grain size range, in terms of equivalent diameter *d*, the diameter of a circular grain with the same area as measured. [4] Percentage of grains with $d > 50$ μm among all grains with $d > 10$ μm, a grain coarseness parameter. [5] Mean Kernal Average Misorientation (KAM) of olivine pixels, 0.05-8° range (omitting zero artifacts below 0.05°, and treating misorientations ≥8° as subgrains). [6] Mean Grain Orientation Spread (GOS), grains of all *d* (±1σ in parentheses). [7] Mean Grain Orientation Spread, grains with $d > 50$ μm (±1σ in parentheses). [8] Mean Grain Orientation Spread, grains with $d < 50$ μm (±1σ in parentheses). [9] Mean Maximum Orientation Spread (MOS), grains with $d > 50$ μm (±1σ in parentheses). [10] Annealing parameter of Ruzicka and Hugo (2018), equivalent to the mean/median ratio of Grain Orientation Spread for grains with $d > 50$ μm. [11] Deformation temperature parameter of Ruzicka and Hugo (2018), equivalent to the fraction of crystal rotation axes in the <010> and <001> crystal directions of olivine for 2-10° misorientations, derived from Crystal Rotation Axis plots (25° halfwidth clustering). [12] Mean Angular Deviation, the average angular mismatch between Kikuchi bands for pixels indexed as olivine and the reference EBSD crystal match file (forsterite, HKL Database in AZtec).

Table 2. Lattice Preferred Orientation (LPO) data for olivine and troilite in Saint-Séverin and Elbert samples (clasts + interclast combined) based on pole figure plots (1 point per grain, all grain sizes, 25° half-width clustering) derived from EBSD LAM data. Δ_i = relative LPO strength of index i, equated to maximum – minimum values of Multiples of Uniform Distribution (MUD).

	Saint-Séverin	Elbert A	Elbert B
troilite $\Delta_{\{0001\}}$	1.09	1.47	3.60
olivine $\Delta_{<100>}$	0.35	0.66	1.69
olivine $\Delta_{<010>}$	0.28	0.67	1.59
olivine $\Delta_{<001>}$	0.36	0.48	0.49
preferred crystallography relationship between troilite and olivine	$<100>_{olivine}$ subparallel to $<0001>_{troilite}$, $<001>_{olivine}$ forms girdle perpendicular to $<0001>_{troilite}$	$<100>_{olivine}$ within ~30° of parallel to $<0001>_{troilite}$	$<010>_{olivine}$ within ~20° of parallel, and <100> within ~20° of perpendicular, to $<0001>_{troilite}$

Table 3. Dislocation TEM data for olivine from Elbert and Saint-Séverin clast and interclast areas.

Area	Olivine grains	Dislocation number density (cm^{-2})	Dislocation Burger's vector **b**	Dislocation character
Elbert Clasts				
FIB1.A	single	1.27×10^{10}	[001] with few [100]	Straight [001] screws with curved loop-ends; planar high-density arrays create misorientations
FIB1.B	single	3.08×10^{9}	[001] with few [100]	Straight [001] screws; planar high-density arrays create misorientations
FIB2.A	single	1.63×10^{9}	[001] with few [100]	Straight [001] screws with straight loop-ends; edge segments in 2 orientations (pencil glide)
Elbert Clast average (ρ_g)*		**4.00×10^{9}**		
Saint-Séverin Clasts				
FIB2.5	multiple	1.60×10^{7}	[001], rare [100]	Curved, loops, one high-density tangle
FIB4.A.2	single	4.15×10^{9}	[001]	Curved, loops, high-density tangles

FIB5.A2.6	single	4.73 x 10^8	[001], few [100]	Curved, loops, possible partial dislocations, subgrain boundary
FIB5.A3.6	single	3.42 x 10^9		Curved, loops, high-density tangles
FIB5.A4.6	single	2.17 x 10^9	[001]	Curved, loops, high-density tangles
Saint-Séverin Clast average (ρ_g)*		**7.47 x 10^8**		
Saint-Séverin Interclast				
FIB6.D.6	multiple	2.73 x 10^9	[001], few [100]	All curved and looped, denser arrays at grain boundaries
FIB6.B.6	multiple	2.70 x 10^9	91% [001], 9% [100]	
FIB7.F.7	multiple	6.56 x 10^9		Curved loops, subgrain boundaries
FIB8.C1.7	multiple	8.02 x 10^9	93% [001], 7% [100]	All curved and looped, denser arrays define grain boundaries
FIB8.B.2	multiple	5.47 x 10^9	[100]	[100] in sub-planar subgrain arrays
FIB8.A.4	multiple	2.63 x 10^9	[100]	[100] in sub-planar subgrain arrays
FIB9.B.1	multiple	8.75 x 10^9	60% [001], 40% [100]	[100] in sub-planar subgrain arrays, [001] curved and loops, high density arrays
Saint-Séverin Interclast average (ρ_g)*		**5.16 x 10^9**		

* Geometric mean.

Figure captions

Fig. 1. Overview images for Saint-Séverin and Elbert samples based on EBSD LAM data. **(a, b)** Saint-Séverin, with Band Contrast (BC) in part a, and clast map in part b (BC as monochrome + All Euler orientation as color). Red lines show principal clast edges and yellow dashes show fracture zones within the clasts. **(c, d)** Elbert A, with Band Contrast (BC) in part c, and clast map in part d (BC as monochrome + All Euler orientation as color). Red lines show principal clast edges and yellow dashes show fracture zones within the clasts. **(e, f)** Elbert B, with Band Contrast (BC) in part e, and clast map in part f (BC as monochrome + All Euler orientation as color). Red lines show principal clast edges and yellow dashes show fracture zones within the clasts. Scalebar = 1 mm in all cases.

Fig. 2. Distribution of shock stages for olivine in **(a)** Elbert (A and B combined) and **(b)** Saint-Séverin, as determined by OM, using the method of Jamsja and Ruzicka (2010). Weighted shock stages is shown at upper right; N = number of grains. The relatively low N for Elbert is caused by fine grain size in this meteorite. Data in part b are the same as in Friedrich et al. (2017), with the weighted shock stage rounded differently.

Fig. 3. Comparison of mesoscale plastic deformation metrics in olivine from Saint-Séverin and Elbert and other type 6 ordinary chondrites, including weighted shock stage *vs.* **(a)** Grain Orientation Spread (GOS) and **(b)** Maximum Orientation Spread (MOS). Elbert A and B are averaged for GOS and MOS. EBSD and OM deformation metrics are well correlated, especially if data for Elbert are excluded. Elbert data are somewhat displaced, which can be explained by the presence of recrystallized grains that have high shock stage (S6) but low GOS and MOS. Data and abbreviations for other meteorites (Friedrich et al., 2017; Ruzicka and Hugo, 2018): PV = Portales Valley (H6/7), Krn = Kernouvé (H6), Prk = Park (L6), MIL = MIL 99301 (LL6), Ldy = Leedey (L6), Brd = Bruderheim (L6), MC = Morrow County (L6).

Fig. 4. EBSD-derived CRA figures (olivine crystal coordinate frame, 25° half-width clustering) for 2-10° misorientations utilizing all olivine EBSD LAM data for **(a)** Saint-Séverin, **(b)** Elbert A, and **(c)** Elbert B, compared to **(d)** a schematic showing corresponding dislocation slip systems (Ruzicka and Hugo, 2018). Colors in parts a through c represent MUD values (redder = higher, bluer = lower), whereas color in part d is related to deformation temperature (warmer/redder colors correspond to higher temperatures, cooler/bluer colors correspond to lower deformation temperatures).

Fig. 5. EBSD-derived troilite and olivine pole figure plots (1 point per grain, all grain sizes, upper hemisphere, 25° halfwidth clustering) for thin-section-scale (LAM) data, including **(a)** troilite in Saint-Séverin (N_g = 2303), **(b)** olivine in Saint-Séverin (N_g = 47513), **(c)** troilite in Elbert A (N_g = 1121), **(d)** olivine in Elbert A (N_g = 20907), **(e)** troilite in Elbert B (N_g = 2120), and **(f)** olivine in Elbert B (N_g = 19888), where N_g = number of grains. Color represents MUD values (redder = higher, bluer = lower). In each sample, troilite shows preferred orientation for {0001}. Olivine shows weaker fabrics that appear to be related to troilite (see Text and Table 2).

Fig. 6. Examples of clast-scale deformation features in olivine and troilite. **(a, b)** Troilite grains in Elbert showing deformation and areas interpreted to represent newly recrystallized grains (e.g., R) within deformed parent crystals. Monochrome base image is band contrast (BC) for all phases, colors are for troilite only and represent Inverse Pole Figure-x (IPFx) orientation (crystal direction in x, or right-left, direction) in part a, and Grain Reference Orientation Deviation (GROD) angle in part b. Recrystallized grains have low values of GROD angle (~0.5°, blue colors) and are bounded by high-angle (>15°) boundaries. The coarse parent grain is especially deformed along internal fractures (e.g., arrow in part a) and its edges (orange areas in part b). Circle in part b indicates location where a fracture cross-cuts a recrystallized grain. LAM map data, Elbert B (2.0 μm step size). **(c)** Partly recrystallized olivine aggregate in Elbert. Monochrome base image is BC for all phases, colors represent GROD angle for olivine only, silver lines are high angle grain boundaries. Recrystallized grains (good examples, R) have GROD angles ~0.5-1° and are bounded by high-angle boundaries, many of which meet in 120° triple junctions, against either deformed or recrystallized grains. Prominent fractures with associated high-GROD-angle areas cut through the aggregate, but mostly not through recrystallized grains. TAM map data, Elbert A, Clast 1, Site 12 (1.0 μm step size). **(d)** Relict chondrule (C) in Saint-Séverin with coarse olivine-rich interior surrounded by orthopyroxene rim, showing more deformation in the chondrule than in the surroundings. Monochrome base image is BC for all phases, colors represent GOS in olivine only. Fracture zones shown by dashed lines. Besides the chondrule, high GOS values occur in small grains associated with fracture zones. TAM data, Saint-Séverin, Clast 3A (1.16 μm step size). **(e, f)** Same field of view of Elbert with BC monochrome base image for all phases, and colors for olivine only representing KAM in part e and GROD angle in part f. Part e shows plastic deformation of olivine associated with microcracking (arrows), and part f shows partial recrystallization of olivine (good examples, R). Silver lines in part f represent high-angle boundaries. Circle in part f indicates location where microcrack cross-cuts a recrystallized grain. High-KAM small grains along bottom in part e are in the interclast area. TAM data, Elbert B, Clast 6, Site 2 (1.0 μm step size). Histograms in parts b through f show the normalized number of pixels or grains with different values of the indicated parameter.

Fig. 7. Clast areas for Elbert (parts a-c) and Saint-Séverin (parts d-f) as seen in TEM WBDF images of olivine. **(a)** Straight c-type screw segments in Elbert with few edge segments visible. Most dislocations are unbound, though one sub-planar tangle containing several a-type dislocations threads the center horizontally. FIB 1 area. **(b)** Long, straight c-type screws with short, straight edge segments. Though dislocations are not clearly associated with discrete planes, the edge and mixed segments are in three discrete directions consistent with {hk0}[001] pencil glide. FIB 2. **(c)** Straight c-type screws with bowed edge segments. Most dislocations are free but a sub-planar pileup of a-type dislocations cuts through many of the c-type dislocations and forms a slight (<1°) misorientation boundary (arrows). FIB1. **(d)** Curved c-type dislocations in Saint-Séverin nucleating at a high angle olivine grain boundary. Several dislocations are in straight screw configuration, but most are highly curved. FIB 5. **(e)** A collection of high-density c-type dislocation tangles in subgrain boundaries. Numerous curved and looped c-type dislocations occupy the space between dislocation tangles. FIB 5. **(f)** Slightly deformed olivine, containing free, mostly curved dislocations, dislocations associated with a high-angle grain boundary (left), and a dislocation tangle around FeS-FeNi inclusions (right). Dislocations are mostly c-type with rare a-type. The inset shows a false color chemical (EDS) map centered on the inclusions, which are arranged in a band. FIB 2.

Fig. 8. Interclast areas for Saint-Séverin. **(a)** A highly deformed field of view for olivine in which most dislocations are associated with sub-planar arrays. Most dislocations are ***c***-type but several isolated ***a***-type dislocations are visible. WBDF TEM image, FIB 3. **(b)** Numerous dislocation loops in olivine formed by cross-slip. At bottom, a high density tangle creates an abrupt misorientation boundary. WBDF TEM image, FIB 6. **(c)** EBSD forescatter Z-contrast context image of FIB 9 area. The interclast region contains primarily olivine (light gray), clinopyroxene (dark gray), and partially maskelynized albite (black). Red box marks the location of parts d and e. **(d)** BC+ olivine GROD angle (0-20° range, same color scheme as Fig. 6c) map of highly deformed interclast grains, showing subgrains. Color indicates the misorientation angle or each pixel with respect to the reference orientation (red = higher value, blue = lower). Red box shows the location of the TEM specimen. High-resolution EBSD map (step size = 0.2 μm). **(e)** BC + olivine KAM (0.1-5° range, same color scheme as in Fig. 6e) map of the same grains as in part d. Green/yellow streaks indicate high-density dislocation arrays that form misorientation (subgrain) boundaries. Red box shows the location of the TEM specimen. **(f)** CRA plots for olivine in Clast 4 adjacent to the interclast region and for the interclast region. Color scale in MUD values for 25° half-width contouring. The interclast area has a slightly lower concentration of <100> rotations consistent with higher-temperature deformation. **(g, h)** WBDF TEM images of olivine seen under different diffraction conditions (red circle marks the same location), showing ***c***-type dislocations in part g, and ***a***-type dislocations in part h. ***a***-type dislocations tend to be located in subgrain boundaries, whereas ***c***-type dislocations tend to be present more outside the boundaries. FIB 9.

Fig. 9. Saint-Séverin (SS) and Elbert (Ebt, averaged A & B) in terms of EBSD deformation temperature parameter and annealing parameter compared to previously studied meteorites (Ruzicka & Hugo, 2018), based on LAM data. Elbert is similar to other high-shock chondrites but with slightly elevated deformation temperature parameter and annealing parameter, whereas Saint-Séverin is unique and characterized by high deformation temperature and low annealing

parameter. Numbers in brackets refer to weighted shock stages. Meteorite abbreviations and symbols same as in Fig. 3.

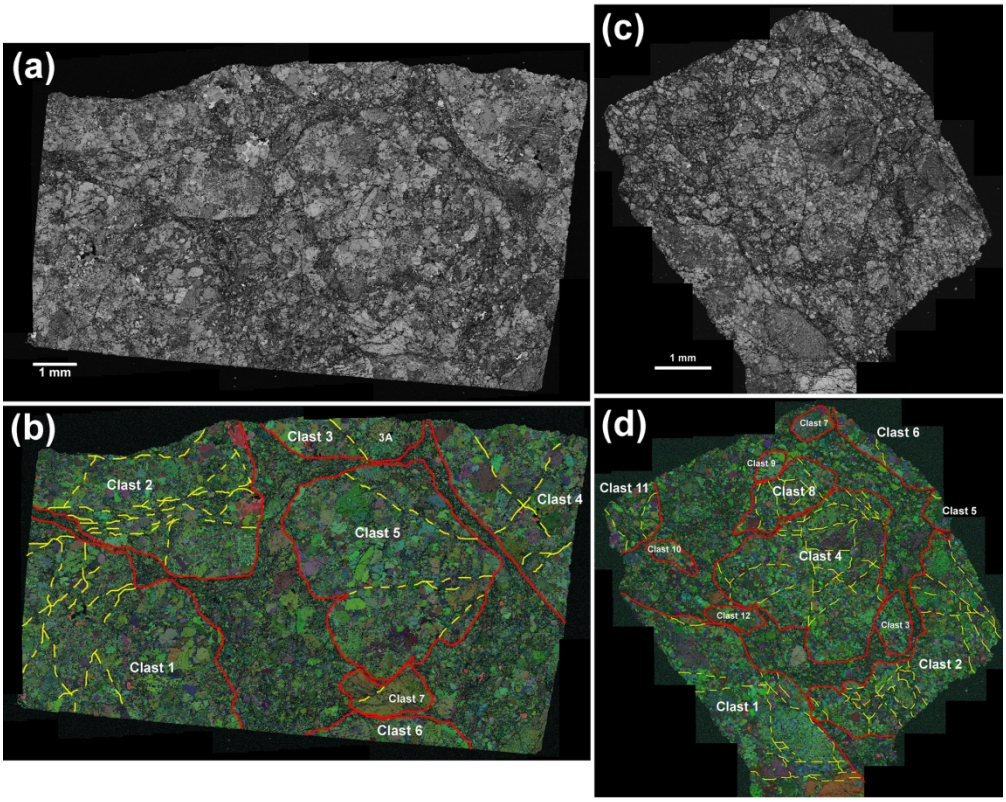

Fig. 1. Overview images for Saint-Séverin and Elbert samples based on EBSD LAM data. (a, b) Saint-Séverin, with Band Contrast (BC) in part a, and clast map in part b (BC as monochrome + All Euler orientation as color). Red lines show principal clast edges and yellow dashes show fracture zones within the clasts. (c, d) Elbert A, with Band Contrast (BC) in part c, and clast map in part d (BC as monochrome + All Euler orientation as color). Red lines show principal clast edges and yellow dashes show fracture zones within the clasts.

175x141mm (300 x 300 DPI)

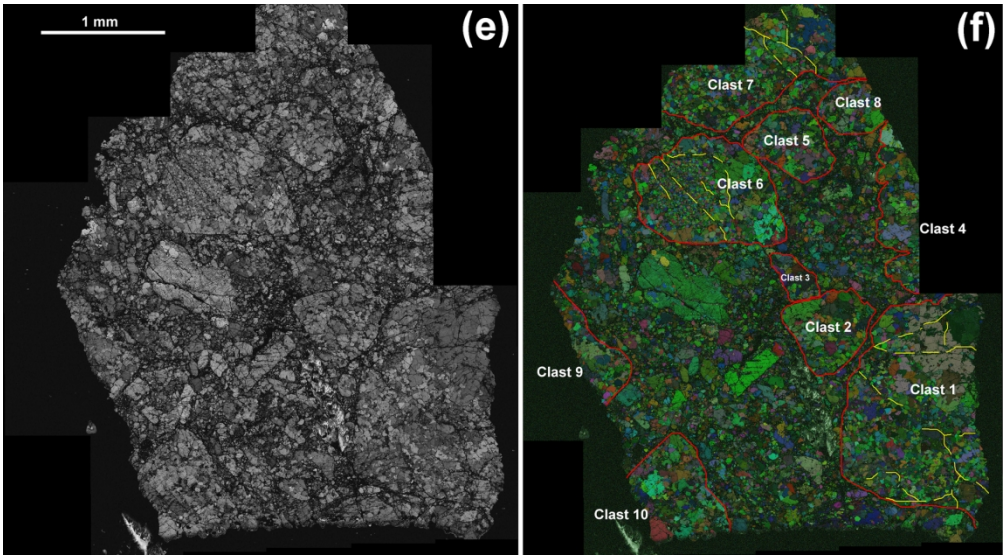

Fig. 1, continued. (e, f) Elbert B, with Band Contrast (BC) in part e, and clast map in part f (BC as monochrome + All Euler orientation as color). Red lines show principal clast edges and yellow dashes show fracture zones within the clasts. Scalebar = 1 mm in all cases.

157x86mm (300 x 300 DPI)

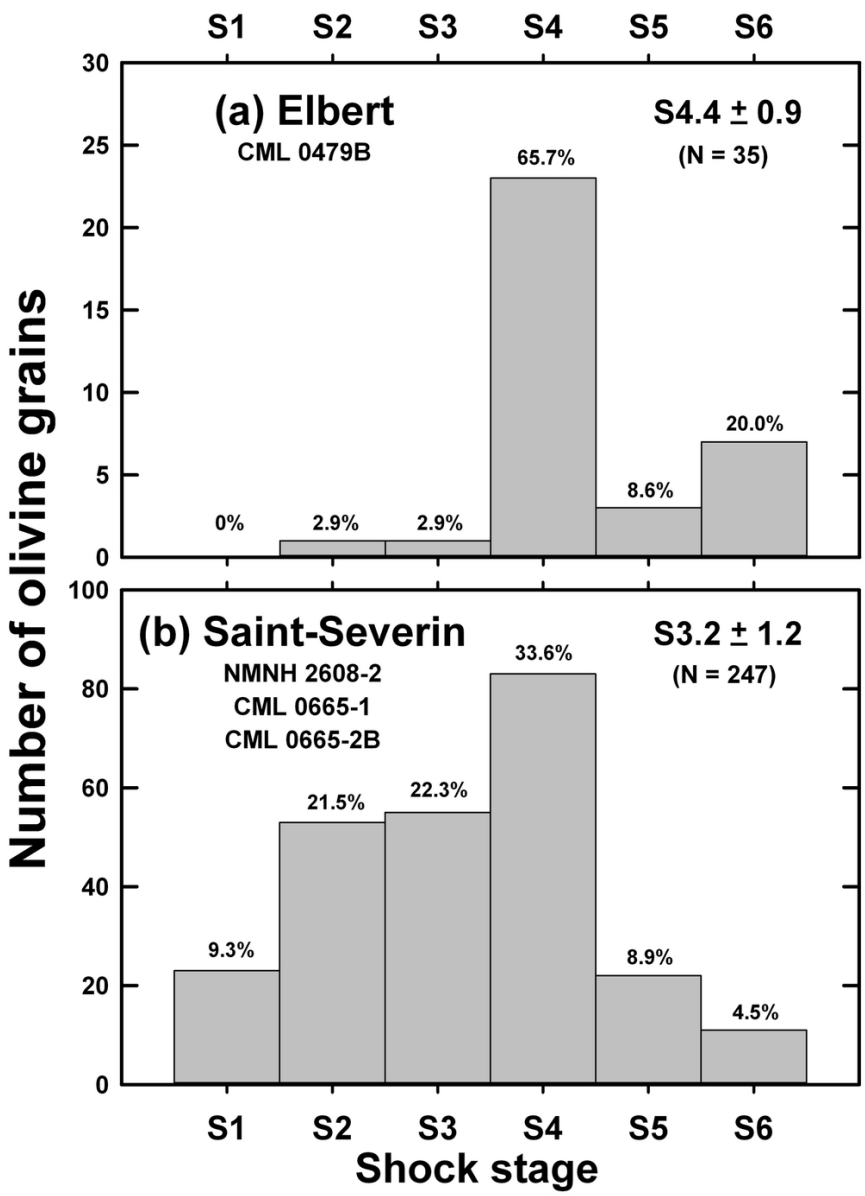

Fig. 2. Distribution of shock stages for olivine in (a) Elbert (A and B combined) and (b) Saint-Séverin, as determined by OM, using the method of Jamsja and Ruzicka (2010). Weighted shock stages is shown at upper right; N = number of grains. The relatively low N for Elbert is caused by fine grain size in this meteorite. Data in part b are the same as in Friedrich et al. (2017), with the weighted shock stage rounded differently.

87x117mm (300 x 300 DPI)

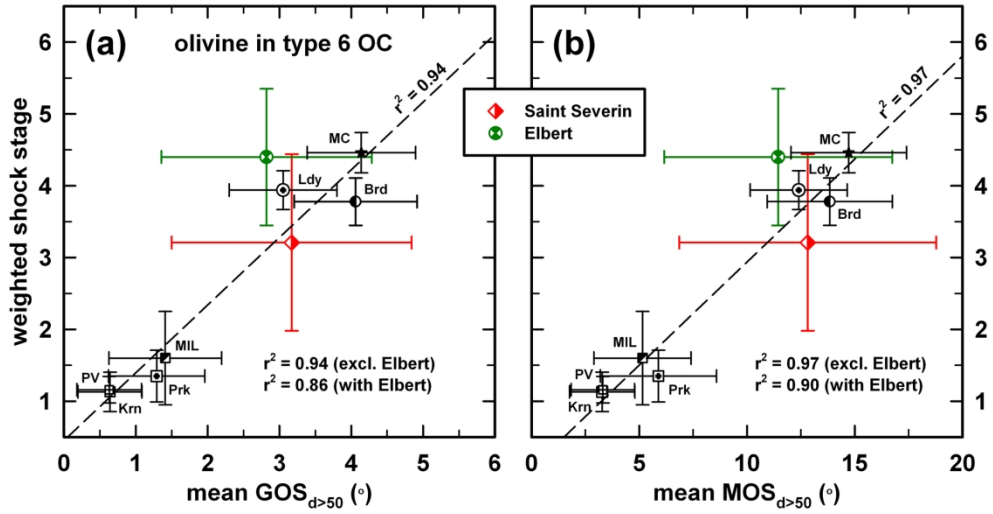

Fig. 3. Comparison of mesoscale plastic deformation metrics in olivine from Saint-Séverin and Elbert and other type 6 ordinary chondrites, including weighted shock stage vs. (a) Grain Orientation Spread (GOS) and (b) Maximum Orientation Spread (MOS). Elbert A and B are averaged for GOS and MOS. EBSD and OM deformation metrics are well correlated, especially if data for Elbert are excluded. Elbert data are somewhat displaced, which can be explained by the presence of recrystallized grains that have high shock stage (S6) but low GOS and MOS. Data and abbreviations for other meteorites (Friedrich et al., 2017; Ruzicka and Hugo, 2018): PV = Portales Valley (H6/7), Krn = Kernouvé (H6), Prk = Park (L6), MIL = MIL 99301 (LL6), Ldy = Leedey (L6), Brd = Bruderheim (L6), MC = Morrow County (L6).

174x93mm (300 x 300 DPI)

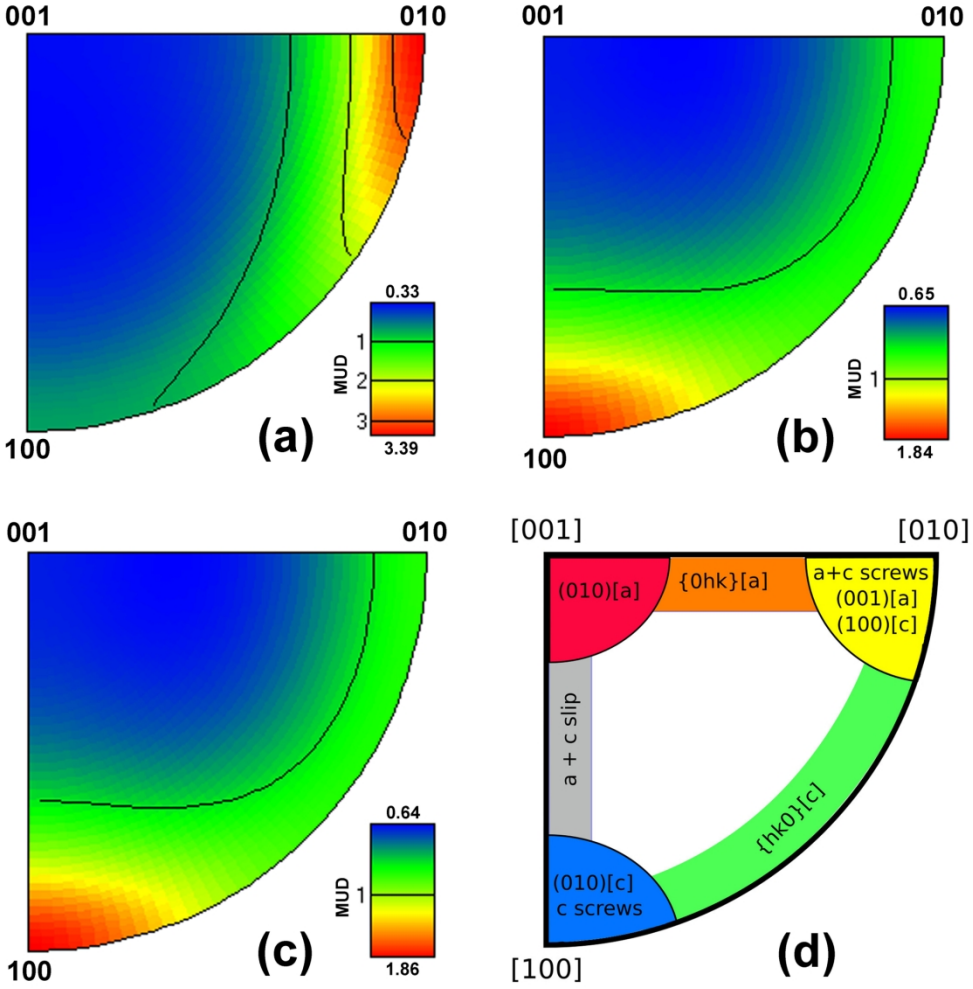

Fig. 4. EBSD-derived CRA figures (olivine crystal coordinate frame, 25° half-width clustering) for 2-10° misorientations utilizing all olivine EBSD LAM data for (a) Saint-Séverin, (b) Elbert A, and (c) Elbert B, compared to (d) a schematic showing corresponding dislocation slip systems (Ruzicka and Hugo, 2018). Colors in parts a through c represent MUD values (redder = higher, bluer = lower), whereas color in part d is related to deformation temperature (warmer/redder colors correspond to higher temperatures, cooler/bluer colors correspond to lower deformation temperatures).

180x180mm (300 x 300 DPI)

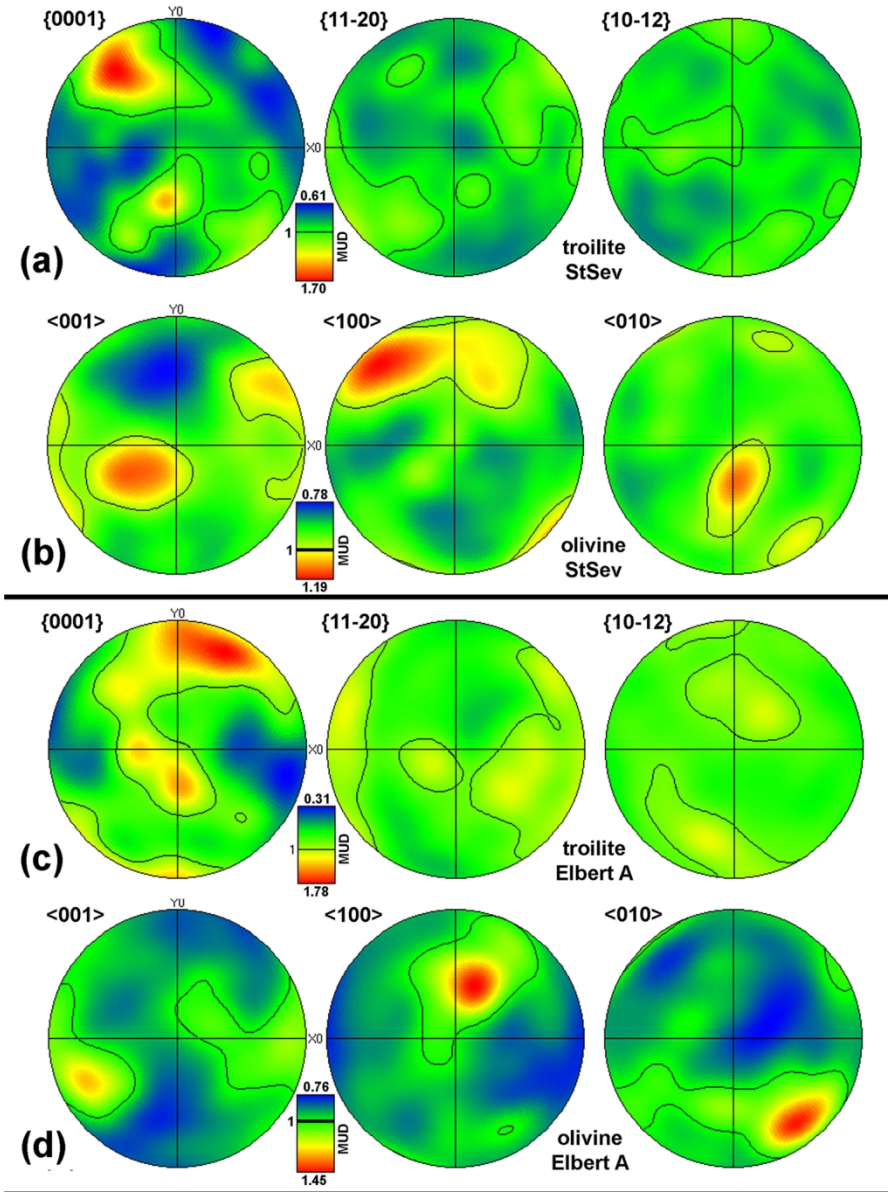

Fig. 5. EBSD-derived troilite and olivine pole figure plots (1 point per grain, all grain sizes, upper hemisphere, 25° halfwidth clustering) for thin-section-scale (LAM) data, including (a) troilite in Saint-Séverin (Ng = 2303), (b) olivine in Saint-Séverin (Ng = 47513), (c) troilite in Elbert A (Ng = 1121), (d) olivine in Elbert A (Ng = 20907).

128x174mm (300 x 300 DPI)

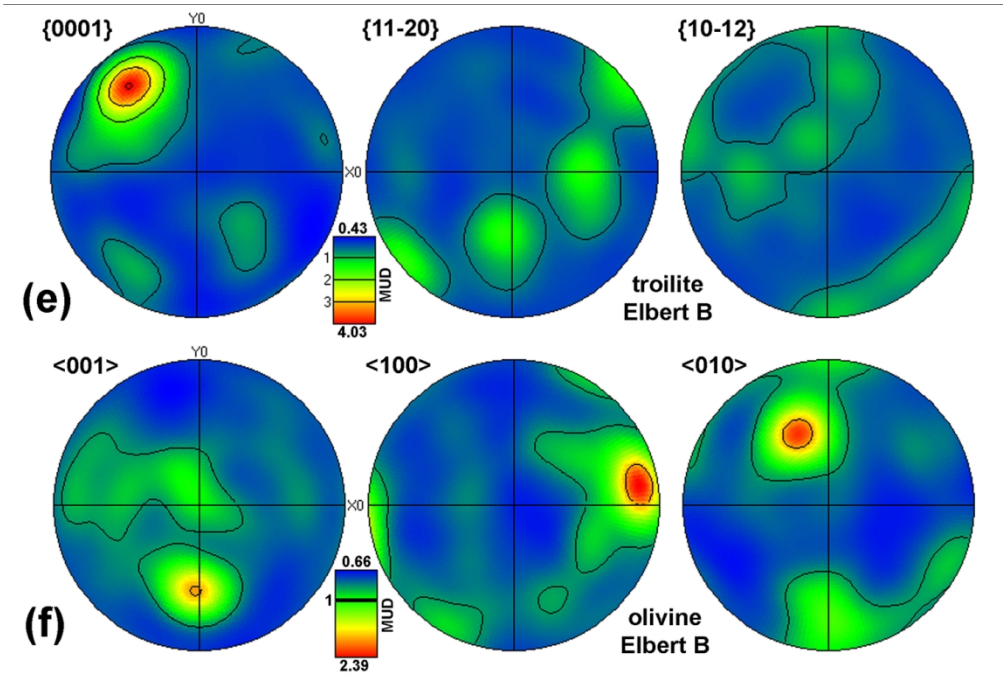

Fig. 5 continued. (e) troilite in Elbert B (Ng = 2120), and (f) olivine in Elbert B (Ng = 19888), where Ng = number of grains. Color represents MUD values (redder = higher, bluer = lower). In each sample, troilite shows preferred orientation for {0001}. Olivine shows weaker fabrics that appear to be related to troilite (see Text and Table 2).

127x86mm (300 x 300 DPI)

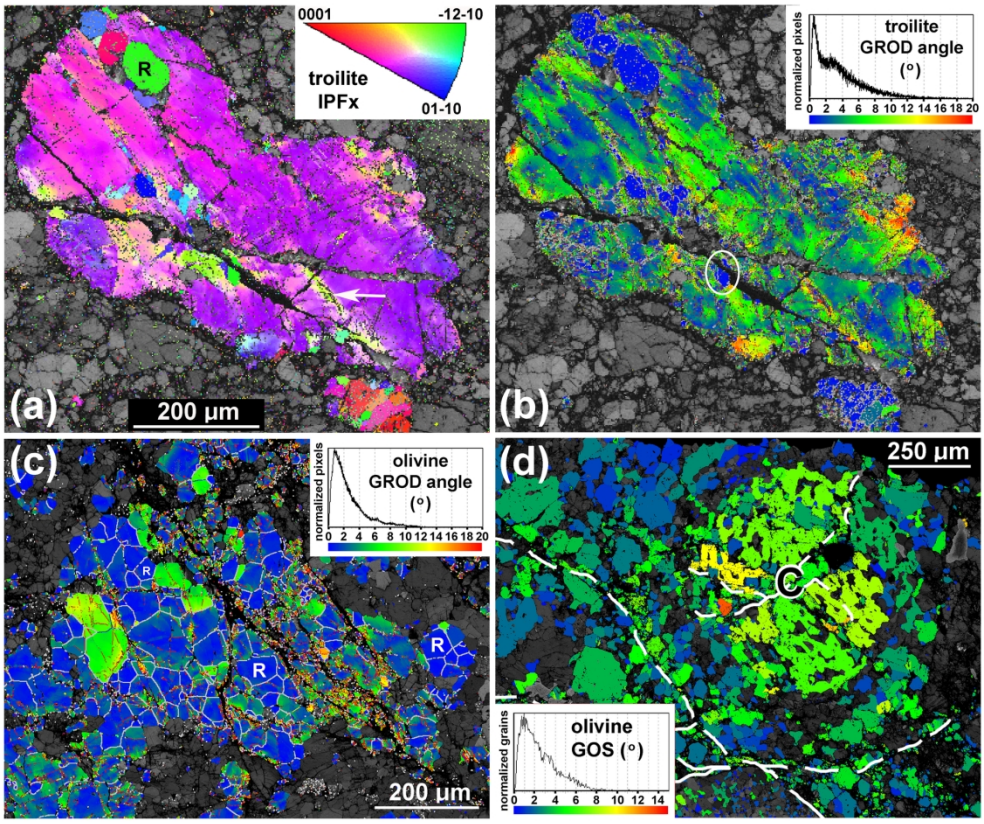

Fig. 6. Examples of clast-scale deformation features in olivine and troilite. (a, b) Troilite grains in Elbert showing deformation and areas interpreted to represent newly recrystallized grains (e.g., R) within deformed parent crystals. Monochrome base image is band contrast (BC) for all phases, colors are for troilite only and represent Inverse Pole Figure-x (IPFx) orientation (crystal direction in x, or right-left, direction) in part a, and Grain Reference Orientation Deviation (GROD) angle in part b. Recrystallized grains have low values of GROD angle (~0.5°, blue colors) and are bounded by high-angle (>15°) boundaries. The coarse parent grain is especially deformed along internal fractures (e.g., arrow in part a) and its edges (orange areas in part b). Circle in part b indicates location where a fracture cross-cuts a recrystallized grain. LAM map data, Elbert B (2.0 µm step size). (c) Partly recrystallized olivine aggregate in Elbert. Monochrome base image is BC for all phases, colors represent GROD angle for olivine only, silver lines are high angle grain boundaries. Recrystallized grains (good examples, R) have GROD angles ~0.5-1° and are bounded by high-angle boundaries, many of which meet in 120° triple junctions, against either deformed or recrystallized grains. Prominent fractures with associated high-GROD-angle areas cut through the aggregate, but mostly not through recrystallized grains. TAM map data, Elbert A, Clast 1, Site 12 (1.0 µm step size). (d) Relict chondrule (C) in Saint-Séverin with coarse olivine-rich interior surrounded by orthopyroxene rim, showing more deformation in the chondrule than in the surroundings. Monochrome base image is BC for all phases, colors represent GOS in olivine only. Fracture zones shown by dashed lines. Besides the chondrule, high GOS values occur in small grains associated with fracture zones. TAM data, Saint-Séverin, Clast 3A (1.16 µm step size).

175x145mm (300 x 300 DPI)

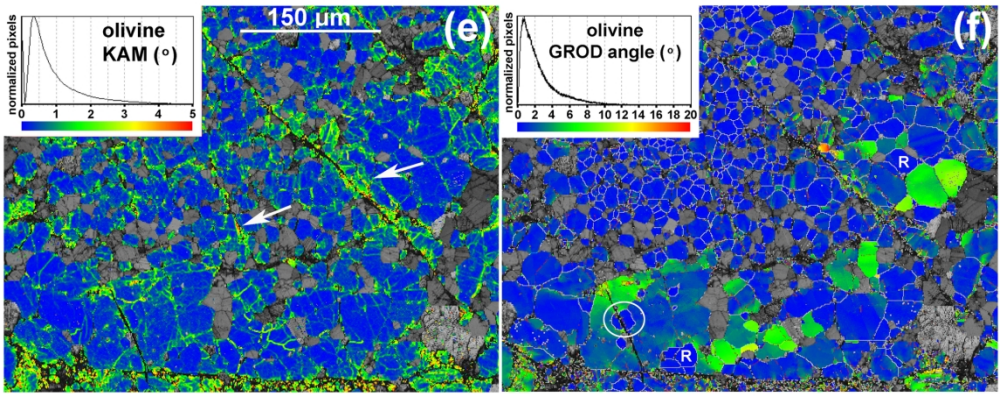

Fig. 6 continued. (e, f) Same field of view of Elbert with BC monochrome base image for all phases, and colors for olivine only representing KAM in part e and GROD angle in part f. Part e shows plastic deformation of olivine associated with microcracking (arrows), and part f shows partial recrystallization of olivine (good examples, R). Silver lines in part f represent high-angle boundaries. Circle in part f indicates location where microcrack cross-cuts a recrystallized grain. High-KAM small grains along bottom in part e are in the interclast area. TAM data, Elbert B, Clast 6, Site 2 (1.0 µm step size). Histograms in parts b through f show the normalized number of pixels or grains with different values of the indicated parameter.

174x69mm (300 x 300 DPI)

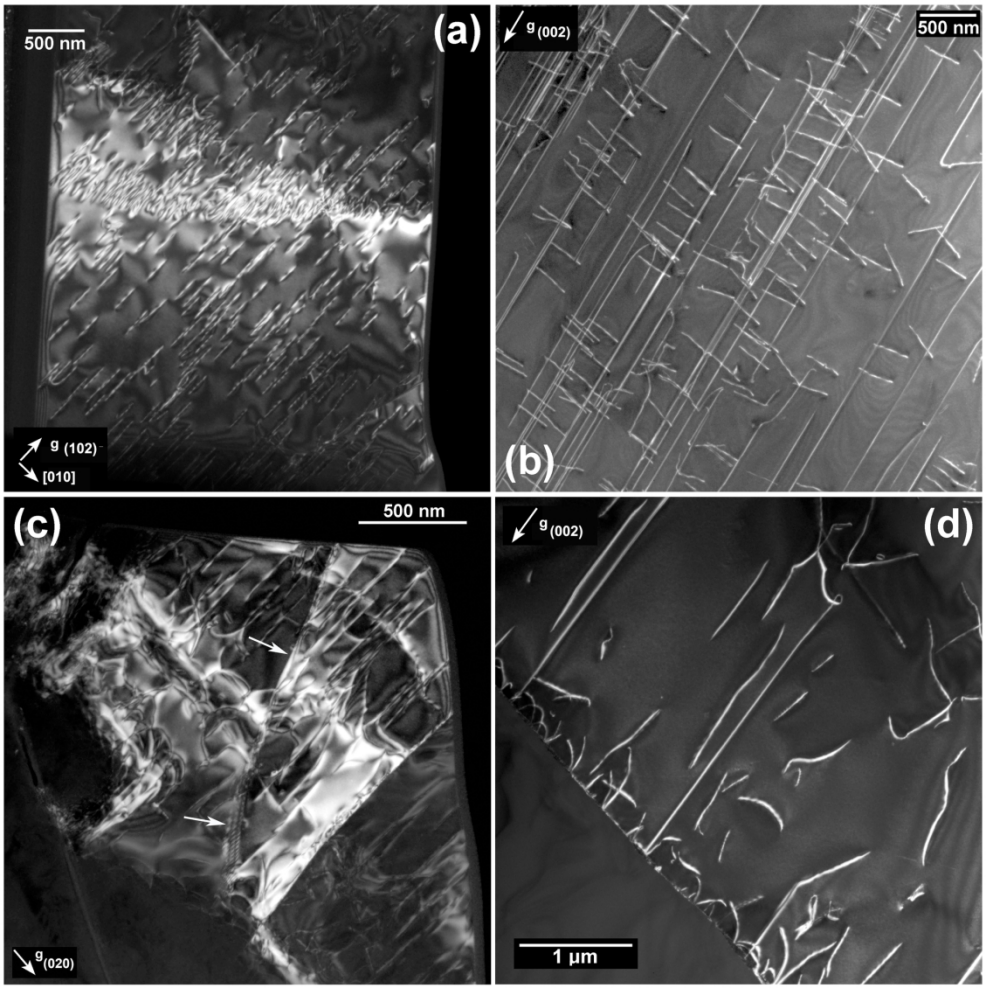

Fig. 7. Clast areas for Elbert (parts a-c) and Saint-Séverin (parts d-f) as seen in TEM WBDF images of olivine. (a) Straight c-type screw segments in Elbert with few edge segments visible. Most dislocations are unbound, though one sub-planar tangle containing several a-type dislocations threads the center horizontally. FIB 1 area. (b) Long, straight c-type screws with short, straight edge segments. Though dislocations are not clearly associated with discrete planes, the edge and mixed segments are in three discrete directions consistent with {hk0}[001] pencil glide. FIB 2. (c) Straight c-type screws with bowed edge segments. Most dislocations are free but a sub-planar pileup of a-type dislocations cuts through many of the c-type dislocations and forms a slight (<1°) misorientation boundary (arrows). FIB1. (d) Curved c-type dislocations in Saint-Séverin nucleating at a high angle olivine grain boundary. Several dislocations are in straight screw configuration, but most are highly curved. FIB 5.

175x175mm (300 x 300 DPI)

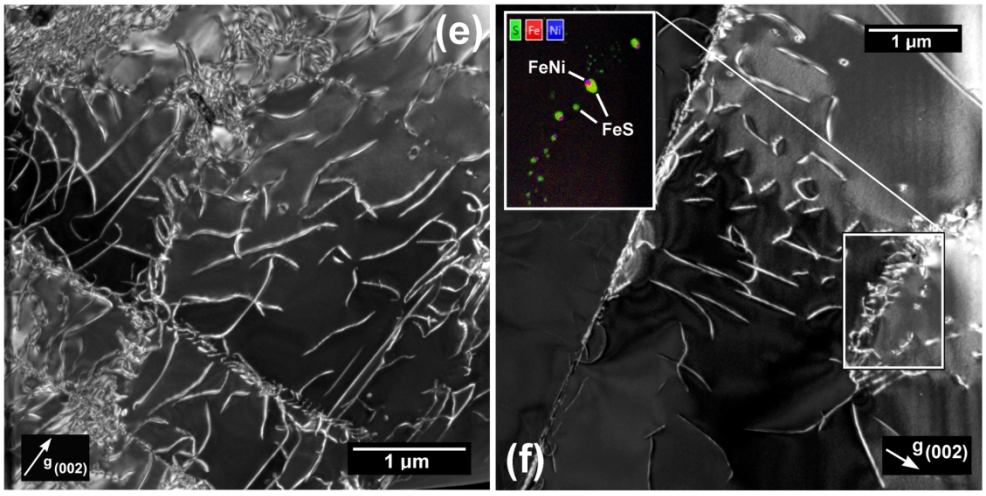

Fig. 7 continued. (e) A collection of high-density c-type dislocation tangles in subgrain boundaries. Numerous curved and looped c-type dislocations occupy the space between dislocation tangles. FIB 5. (f) Slightly deformed olivine, containing free, mostly curved dislocations, dislocations associated with a high-angle grain boundary (left), and a dislocation tangle around FeS-FeNi inclusions (right). Dislocations are mostly c-type with rare a-type. The inset shows a false color chemical (EDS) map centered on the inclusions, which are arranged in a band. FIB 2.

175x88mm (300 x 300 DPI)

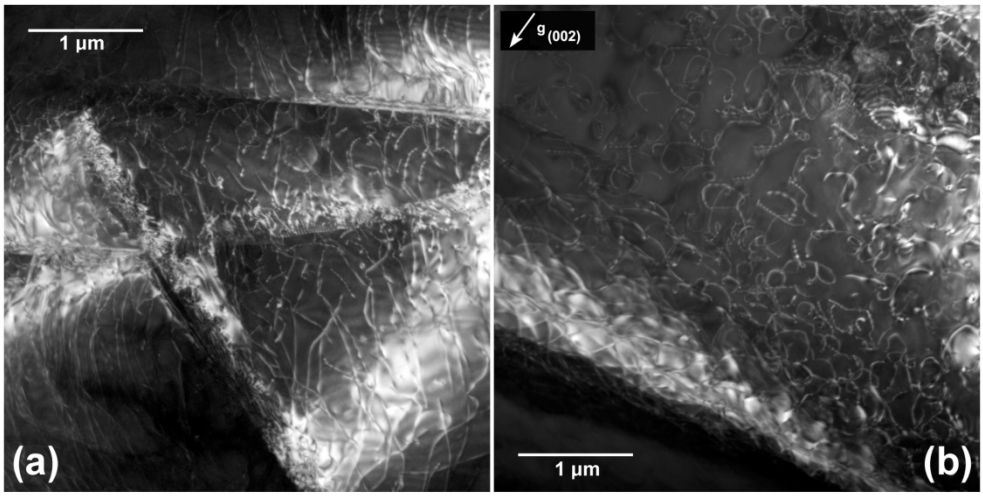

Fig. 8. Interclast areas for Saint-Séverin. (a) A highly deformed field of view for olivine in which most dislocations are associated with sub-planar arrays. Most dislocations are c-type but several isolated a-type dislocations are visible. WBDF TEM image, FIB 3. (b) Numerous dislocation loops in olivine formed by cross-slip. At bottom, a high density tangle creates an abrupt misorientation boundary. WBDF TEM image, FIB 6.

180x90mm (300 x 300 DPI)

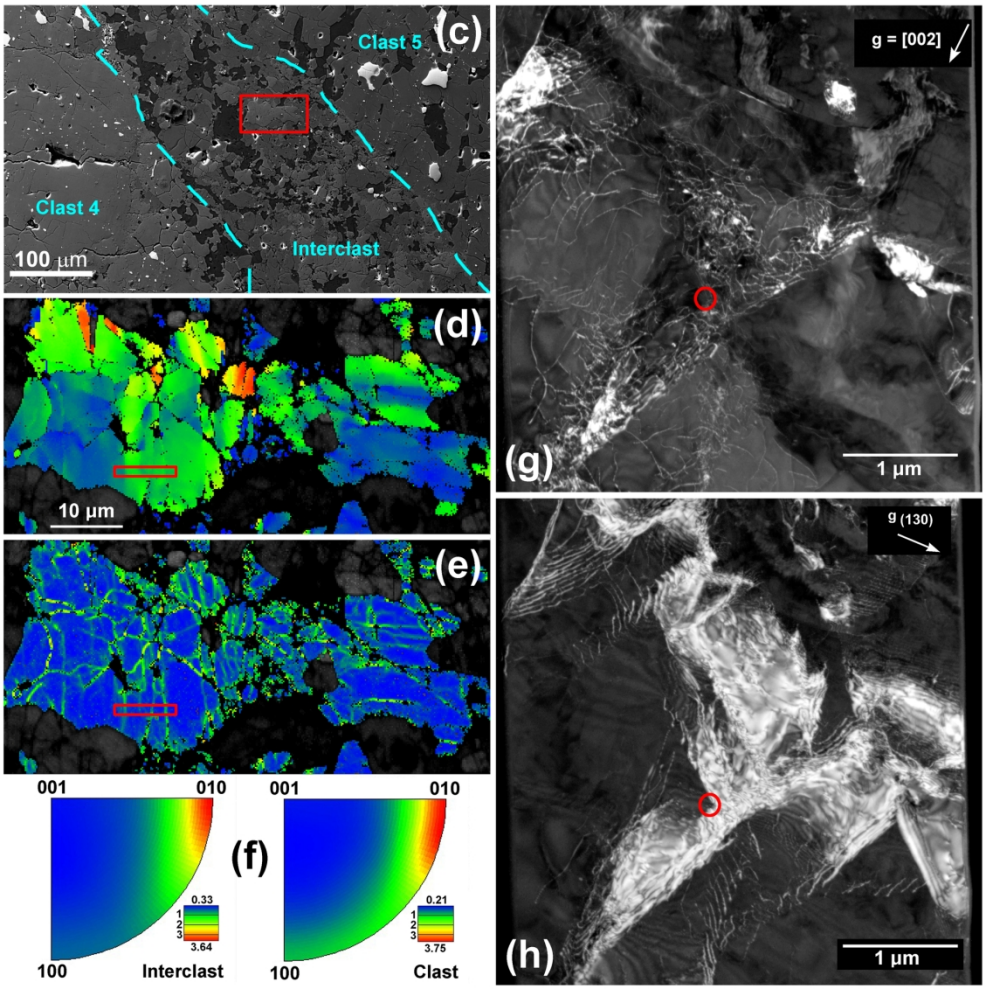

Fig. 8 continued. (c) EBSD forescatter Z-contrast context image of FIB 9 area. The interclast region contains primarily olivine (light gray), clinopyroxene (dark gray), and partially maskelynized albite (black). Red box marks the location of parts d and e. (d) BC+ olivine GROD angle (0-20° range, same color scheme as Fig. 6c) map of highly deformed interclast grains, showing subgrains. Color indicates the misorientation angle or each pixel with respect to the reference orientation (red = higher value, blue = lower). Red box shows the location of the TEM specimen. High-resolution EBSD map (step size = 0.2 µm). (e) BC + olivine KAM (0.1-5° range, same color scheme as in Fig. 6e) map of the same grains as in part d. Green/yellow streaks indicate high-density dislocation arrays that form misorientation (subgrain) boundaries. Red box shows the location of the TEM specimen. (f) CRA plots for olivine in Clast 4 adjacent to the interclast region and for the interclast region. Color scale in MUD values for 25° half-width contouring. The interclast area has a slightly lower concentration of <100> rotations consistent with higher-temperature deformation. (g, h) WBDF TEM images of olivine seen under different diffraction conditions (red circle marks the same location), showing c-type dislocations in part g, and a-type dislocations in part h. a-type dislocations tend to be located in subgrain boundaries, whereas c-type dislocations tend to be present more outside the boundaries. FIB 9.

175x175mm (300 x 300 DPI)

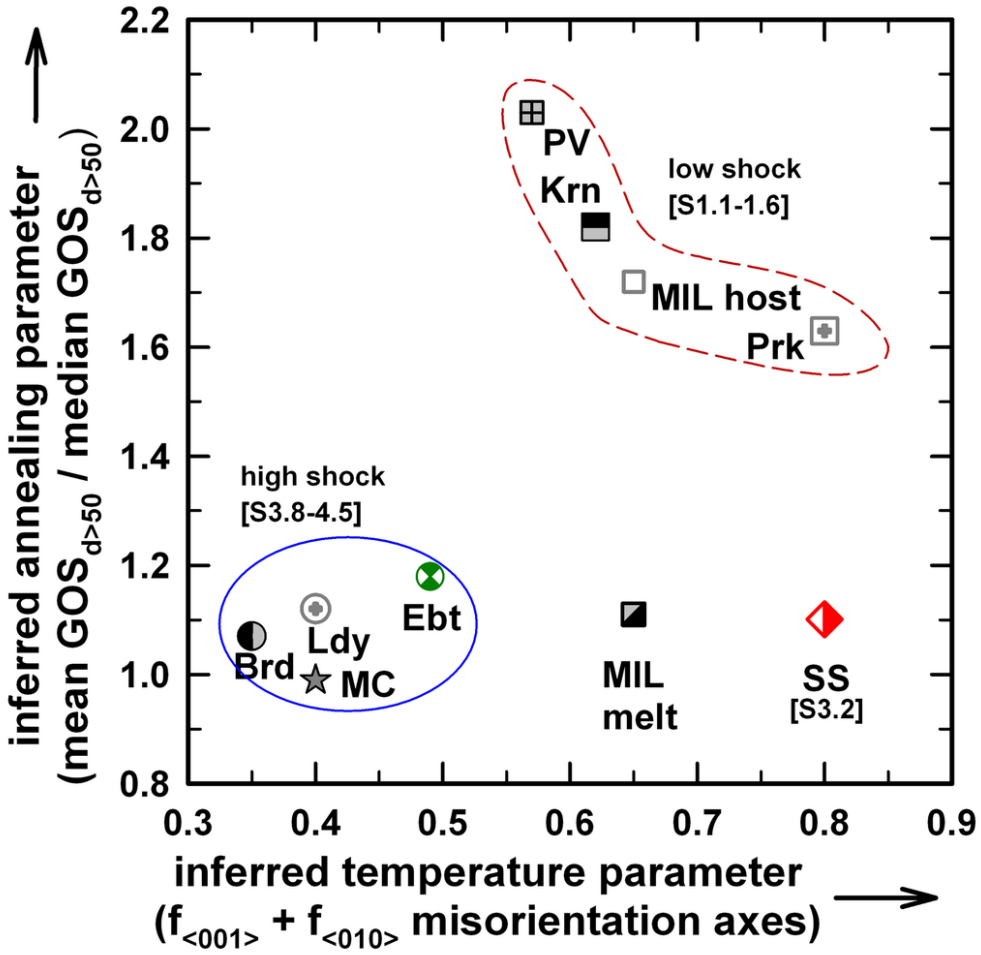

Fig. 9. Saint-Séverin (SS) and Elbert (Ebt, averaged A & B) in terms of EBSD deformation temperature parameter and annealing parameter compared to previously studied meteorites (Ruzicka & Hugo, 2018), based on LAM data. Elbert is similar to other high-shock chondrites but with slightly elevated deformation temperature parameter and annealing parameter, whereas Saint-Séverin is unique and characterized by high deformation temperature and low annealing parameter. Numbers in brackets refer to weighted shock stages. Meteorite abbreviations and symbols same as in Fig. 3.

87x86mm (300 x 300 DPI)